Lamb shift measurement in the $1\,^1S$ ground state of helium

K. S. E. Eikema, W. Ubachs, W. Vassen, and W. Hogervorst
Laser Centre Vrije Universiteit, Department of Physics and Astronomy, De Boelelaan 1081, 1081 HV Amsterdam, The Netherlands
(Received 5 August 1996)

With a phase-modulated extreme ultraviolet pulsed laser source the frequency of the $1\,^1S$-$2\,^1P$ transition of helium at 58 nm has been measured. The phase modulation scheme enabled measurement and reduction of frequency chirp, usually limiting pulsed precision spectroscopy. From the measured transition frequency of 5 130 495 083(45) MHz, a fourfold improved value of the ground state Lamb shift of 41 224(45) MHz is deduced, in good agreement with a theoretical value of 41 233(35) MHz based on QED calculations up to order $\alpha^5 Z^6$. From these measurements, the well-known binding energy of the $2\,^1P$ state and the previously determined ^{4}He-^{3}He isotope shift, accurate values for the ionization energies of the helium atom follow: 198 310.6672(15) cm^{-1} for ^{4}He and 198 301.8808(15) cm^{-1} for ^{3}He. [S1050-2947(97)05403-6]

PACS number(s): 32.30.Jc, 12.20.Fv, 42.65.Ky

I. INTRODUCTION

Fifty years ago Lamb and Retherford found that the $2\,^2S_{1/2}$-$2\,^2P_{1/2}$ levels in atomic hydrogen are not degenerate as predicted by Dirac theory [1,2]. This observation, a splitting of $\sim$1 GHz, marked the start of intense theoretical activity, resulting in the development of quantum electrodynamics (QED). Since then the ''Lamb shift'' denotes energy contributions due to QED effects (including some higher-order relativistic effects). Tests of atomic theory including quantum electrodynamic (QED) effects are now possible for an increasing number of systems. Until recently, accurate tests of QED calculations could be performed only in the most simple atoms such as hydrogen and positronium. For these systems the non-QED energy structure can be calculated with high precision using relativistic quantum mechanics. The most important contributions to the Lamb shift are the self-energy and vacuum polarization (see, e.g., [3]). An increasing number of smaller contributions can be calculated nowadays such as, e.g., two-loop virtual photon exchange [4]. As the main QED effects scale with $1/n^3$(n is the principal quantum number) and are only large in S states, the Lamb shift is largest in the ground state. Developments in laser technology enabled Lamb shift measurements in the $1\,^2S_{1/2}$ ground state of hydrogen, applying two-photon Doppler-free excitation to $2\,^2S_{1/2}$ and $3\,^2S_{1/2}$. The results surpass the accuracy of the best RF measurements on the $2\,^2S_{1/2}$-$2\,^2P_{1/2}$ transition [5,6]. In these precision experiments the size of the proton rather than the understanding of QED is becoming the limiting factor. In fact these measurements can be interpreted to provide a new value for the proton radius [5,6].

Although analytical non-QED calculations are impossible for any system with more than two particles, recent calculations based on a variational approach in helium and helium-like ions with low Z are now sufficiently accurate to be regarded as exact for all practical purposes [3,7]. The accuracy of these variational calculations in helium was confirmed by a nonvariational solution of the Schrödinger equation based on the correlation function hyperspherical-harmonic method [8]. Therefore experimental transition frequencies can be used to test QED calculations also for helium. QED effects in helium are more complex than in hydrogen. Compared to hydrogen the one-electron contribution (denoted $E_{L(1)}$) to the Lamb shift in helium is reduced due to mutual shielding of the nucleus by the two electrons. In addition, a contribution due to a proximity effect of the electrons is present ($E_{L(2)}$), for which no equivalent in hydrogen exists. Helium is therefore an interesting system for QED tests when measuring absolute transition frequencies.

Measurements of the Lamb shift in helium mainly concentrated on the $2\,^3S$ and $2\,^1S$ states. Most accurate results were obtained for $2\,^3S$ [9,10]. However, the interesting two-electron contribution to the Lamb shift is ten times larger for ^1S states because of the larger spatial overlap of both electrons in singlet states. Recently two groups excited $1snp$ [11] and $1snd$ states [12] with CW lasers starting from $2\,^1S$. Values of 2810.57(21) MHz and 2809.92(15) MHz, respectively, for the $2\,^1S$ Lamb shift are deduced from these measurements [13]. Initially a large discrepancy of 93 MHz with theory was found [13], which was largely resolved in a reevaluation of the Bethe logarithm by Baker *et al.* [14]. Both experimental values are now in reasonable agreement with the most recent theoretical value of 2808.48 MHz, which has an uncertainty of 1 MHz from uncalculated higher-order terms of $O(\alpha^4 Z^4)$ and 0.18 MHz due to the Bethe logarithm [13]. However, in the calculation of relativistic corrections of $O(\alpha^4 Z^5)$ to the lowest-order Lamb shift of size -51.44 MHz an approximation was made for a two-electron shielding effect that has not yet been proven rigorously. Also higher-order terms are expected to contribute at the 1 MHz level.

As in hydrogen, the Lamb shift of helium is more than an order of magnitude larger in its ground state. Theoretically a Lamb shift of 1.3754 cm^{-1}, including a two-electron contribution of -0.1404 cm^{-1}, has been calculated [15,16]. The study of the $1\,^1S$ ground state is difficult due to its large energy separation from the excited states ($>160\,000$ cm^{-1}). Therefore an investigation of the $1\,^1S$ state presents an experimental as well as a theoretical challenge. For a long time the most accurate data on the ground state were those obtained with classical spectroscopy. In 1958 Herzberg used a helium discharge in combination with

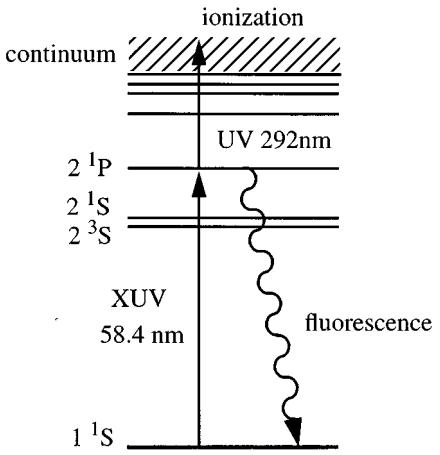

FIG. 1. Detection principle of the $1\,^1S$-$2\,^1P$ transition in helium in a 1 XUV photon excitation followed by a 1 UV photon ionization scheme. The 1 XUV + 1 UV two-photon ionization competes with resonant fluorescence to the ground state; fluorescence decay to $2\,^1S(<0.1\%)$ is neglected.

a 3 m spectrograph to measure the wavelength of the $1\,^1S$-$2\,^1P$ transition at 58.4 nm [17]. He obtained an absolute accuracy of 0.15 cm^{-1} for the $1\,^1S$ binding energy. The $1\,^1S$-$2\,^1P$ transition isotope shift for ^{3}He-^{4}He was determined in the same setup to be 264.6(1.8) GHz.

Since the classical experiment of Herzberg, considerable progress has been made in extreme ultraviolet (XUV) spectroscopy. Narrow-band laser radiation at wavelengths >70 nm is now routinely produced by third-order nonlinear up-conversion in gases and metal vapors, using high-power visible and ultraviolet laser pulses [see, e.g., 18–20]. Higher-order up-conversion with short-pulse lasers (down to a few tens of fs) has been demonstrated and radiation at wavelengths as short as 0.7 nm has been generated [21]. Short pulses, however, possess an inherently large Fourier transformed bandwidth which is not favorable for high-resolution experiments in the frequency domain.

In recent Letters [22,23] we reported precision measurements of the $1\,^1S$ Lamb shift in helium. In a first study [22] the $1\,^1S$-$2\,^1P$ transition was excited by a pulsed dye laser based XUV-radiation source of bandwidth 0.3 cm^{-1} at 58 nm. Production of XUV radiation was based on fifth harmonic up-conversion of the frequency-doubled output of a dye-laser system at 584 nm with nanosecond laser pulses. The XUV-induced $1\,^1S$-$2\,^1P$ resonance line was detected by photoionization with UV pulses (see Fig. 1). An advantage of harmonic up-conversion is that calibration is possible in the visible, where accurate frequency standards are available. As a result, the ground state Lamb shift was determined with an accuracy of 1 GHz, which meant a factor of 5 improvement over the value of Herzberg [17]. In this pionering experiment the bandwidth of the XUV-laser source turned out to be the limiting factor. This led to the replacement of the dye laser by a more narrow-band pulsed-dye-amplifier (PDA) system. This home-built high power PDA system was successfully employed to measure the same $1\,^1S$-$2\,^1P$ transition in helium resulting in an accuracy for the ground state Lamb shift of 175 MHz [23], which was again a fivefold improvement over the first study. Also the ^{4}He-^{3}He transition isotope shift on the $1\,^1S$-$2\,^1P$ resonance line was studied with the PDA system resulting in an accurate value of 263 410(7) MHz.

Precision measurements with pulsed laser sources are generally hampered by time-dependent frequency deviations (chirp) resulting from phase fluctuations in PDA's [24,25]. This phenomenon may significantly limit the accuracy of frequency calibration in precision studies using pulsed laser sources. Indeed chirp was the limiting factor in our second study on the helium ground state Lamb shift [23]. Early experiments on hydrogen [26] and positronium [27] were limited in much the same way, before cw laser excitation was achieved [28,29]. Many experiments, however, can at present only be performed by pulsed excitation. As a result, the study of frequency chirp has become an active field of research.

In this paper we present a method to accurately measure the chirp effects on laser pulses as short as 6 ns. Moreover a method is described to actively control and eliminate the chirp effects using an electro-optic modulator to produce ''antichirped'' pulses. Applying these electro-optical techniques we demonstrate that chirp-induced calibration errors in XUV spectroscopy can be eliminated to a large extent. In combination with methods to address the phenomenon of dynamic Stark shifts and an improved calibration standard, this results in a determination of the Lamb shift with an accuracy 45 MHz, again a fourfold improvement over the previous value [23]. A detailed account will be given of the experimental techniques that were used to determine the accurate value for the $1\,^1S$ ground Lamb shift in helium as well as the ^{4}He-^{3}He transition isotope shift in the $1\,^1S$-$2\,^1P$ resonance line. Also the dynamic Stark-shift calculations for both isotopes, which were not published in full before, will be presented.

II. EXPERIMENTAL SETUP

The setup consists of three functional parts (Fig. 2). In the first part a narrow bandwidth carrier frequency at 584 nm is generated and accurately calibrated using an etalon and saturation spectroscopy. This part will be described in Sec. II A. The second stage consists of a pulse-dye amplifier (PDA) and frequency doubler to generate high-power UV pulsed radiation at 292 nm. Chirp induced in the PDA is monitored and modified in this part of the setup, which is detailed in Sec. II B. In the third part the UV is up-converted to XUV radiation at 58.4 nm by a fifth-harmonic process, which then induces the $1\,^1S$-$2\,^1P$ resonance line in helium in a crossed-beam setup (Sec. II C).

A. Primary light source and calibration

The primary source of radiation is a Spectra-Physics 380D cw ring laser with Rhodamine 6G dye (output 700 mW, $\sim$1 MHz bandwidth). In the harmonic up-conversion process the frequency relation $f_{\mathrm{XUV}} \sim 10 f_{\mathrm{cw}}$ (apart from small deviations which are discussed in Sec. III) holds, so the calibration of the $1\,^1S$-$2\,^1P$ transition frequency can be performed in the visible using saturation spectroscopy on molecular iodine (Fig. 3). For this purpose the ''o'' component of the P(88)15-1 transition in I_2, close to $\frac{1}{10}$th of the

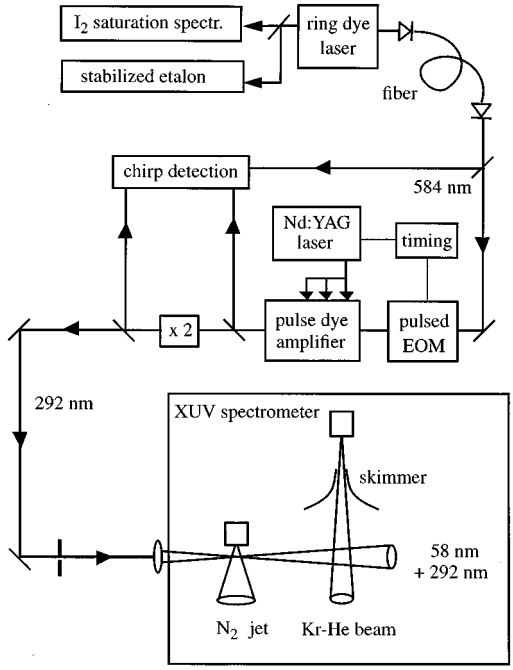

FIG. 2. Overview if the experimental setup to measure the $1\,^1S$-$2\,^1P$ transition in helium (EOM, electro-optic modulator; AOM, acousto-optic modulator). The box in the lower right contains the vacuum setup for XUV generation, further detailed in Fig. 5.

$1\,^1S$-$2\,^1P$ frequency, was calibrated in our laboratory using saturation spectroscopy (see also Sec. IV) relative to the ''i'' component of the R(99)15-1i transition in I_2 [30]. The saturating beam of 5 mW, mechanically chopped at 850 Hz, is focused with a 1 m lens in a 10 cm long iodine cell at room temperature. The saturation signal is recorded with a weak probe beam (0.2 mW). A bandpass filter with 0.07 sec integration time was used to select the saturation signal at 850 Hz. The energy separation of almost 13 cm^{-1} between these two hyperfine components was measured using a sealed and temperature stabilized ($\sim 0.1°C$) etalon. In addition, this etalon is actively locked to an I_2-stabilized HeNe laser, resulting in negligible drift during the measurements. The free

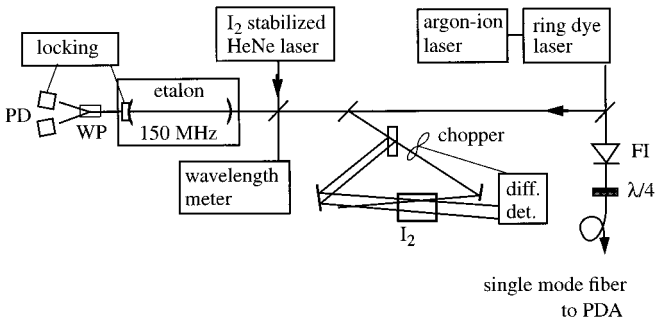

FIG. 3. Setup for calibration of the seed laser (ring dye laser) in the visible. Relative calibration is performed with the etalon that is length stabilized using an I_2 frequency locked HeNe laser. Absolute calibration is obtained by recording an I_2 saturation signal (PD, photodiode; WP, Wollaston prism; FI, Faraday isolator; PDA, pulse dye amplifier).

spectral range (FSR) of this etalon of 148.9567(4) MHz was determined using I_2 hyperfine lines [30,31] within a few hundred cm^{-1} from the P(88)15-1. No significant wavelength dependence of the FSR was found over $\pm 300\ cm^{-1}$ around our calibration position.

The calibration standard was measured by Grieser *et al.* [30] at 6 °C while we used 20 °C. Comparison of the frequency of this transition at temperatures of 0 °C (cell partly in ice water) and 20 °C showed that the uncertainty due to this temperature difference is smaller than 0.4 MHz. Pressure shifts may also arise from leakage of air into the I_2 cell. Therefore the difference between the standard sealed cell and one that can be evacuated and refilled in a few minutes was also measured. The influence of up to ~ 0.01 mbar of air on the reference lines was investigated and no difference was found within an uncertainty of 0.3 MHz. Additional tests on the influence of dynamic Stark shift, magnetic field, and electronic integration time (0.07 sec) resulted in a conservative estimate for the uncertainty in the position of both lines of ~ 1 MHz. Together with the uncertainty in the difference measurement with the etalon (1 MHz due to 2563 fringes) an estimated total rms uncertainty of 1.7 MHz for the P88(15-1)-o line at 513 049 427.1 MHz results. The small interval of ~ 84 MHz in the visible to the resonance position of $1\,^1S$-$2\,^1P$ introduces no significant additional error. Therefore the XUV frequency uncertainty due to the absolute calibration in the visible is 17 MHz (see Table I).

B. The pulse dye amplifier

Tunable 58 nm radiation with a pulse length of a few nanoseconds is generated in a fifth-harmonic process from ultraviolet light at 292 nm. Due to the low nonlinear efficiency high laser powers are required. The requirements for beam-pointing stability are stringent because of calibration errors induced by Doppler effects. With these two requirements in mind a high-power PDA system was built, as shown in Fig. 4 (the boxes indicating the PDA chirp modification and measurement components are described in Sec. III B).

A single-mode fiber (25 m long) is used to decouple the cw ring laser from the PDA, ensuring a good pointing stability. A Faraday isolator is inserted to prevent disruption of the cw laser by backreflections from the fiber. The fiber does not preserve polarization, and therefore the polarization may be scrambled because of temperature changes and mechanical stress. However, the PDA and the harmonic conversion processes require stable linear polarization. Therefore, a second Faraday isolator at the fiber exit serves two purposes. It protects the fiber exit from being damaged by backscattered and amplified PDA radiation and it selects the linear, vertical polarization component. Twisting of the fiber in combination with two quarter-wave plates is used to maintain linear polarization and optimal seed power.

The PDA is pumped by an injection-seeded and frequency-doubled 10 Hz Nd:YAG laser (Spectra Physics GCR-5) delivering 740 mJ at 532 nm. Amplification of 150 mW cw laser light to 6.5 ns pulses of 220 mJ takes place in three rectangular dye flow cells, mounted under Brewster angle to minimize losses. All cells contain Rhodamine B. The first cell (optical length 15 mm, 45 mg/l) is transversely

TABLE I. Experimental and theoretical values for the $1\,^1S$-$2\,^1P$ isotope shift ^{4}He-^{3}He and for the transition frequency of ^{4}He. All values in MHz (1σ error).

	Isotope shift		Transition frequency	
Measured	263 416	(5)	5 130 495 110	(5)
Corrections				
Chirp : measurement analysis	0		0[a]	(14)
PDA beam inhomogeneities	0		0	(20)
fifth harmonic, measured	0		10	(13)
Stark shift	−6	(3)	−44	(15)
Doppler shift	0	(2)	7	(20)
drift (systematic)	0			(3)
Line shape	0	(3)	0	(3)
Calibration 584 nm	0	(1)	0	(17)
Corrected value; experimental	263 410	(7)	513 0495 083	(45)
Theory	263 411.26	(0.11)	513 0495 074	(35)

[a]Already included in ''Measured.''

pumped with 10 mJ from a quartz wedge reflection. Two cylindrical lenses and a diaphragm are used to illuminate the amplification zone homogeneously. The seed beam is focused to a diameter of only a few tenths of a mm just behind the quartz window of the first dye cell. In this way the PDA output saturates at relatively low seed power ($\sim$50 mW), and spatial variation of the gain (10^4–10^5) over the seed beam diameter is kept to a minimum. The optical path of the amplified beam through the PDA is folded, as shown in Fig. 4, to allow for 2 m and 1.3 m distances between the amplifier cells. Together with a diaphragm (diameter 3 mm) just before the second stage, spontaneous amplified emission is in this way kept below 1% without any further measures. In contrast to previous designs (e.g., [20]) both the second and third amplifier are longitudinally pumped (in opposite direction to the seed beam). This geometry is more efficient than side pumping because it allows the pump power to be distributed unevenly over the cell to match the power needed by the amplified beam as it propagates through the gain medium. Optimum power is generated for a dye solution of about 15 mg/l Rh B in the second and last stage, which therefore share the same circulation pump. Spatial filtering of the amplified beam is used before the second stage only (80 μm pinhole) to remove diffracted beams from the first cell. No further spatial filtering is necessary after the second and third amplifier cell because of the good beam quality of the Nd:YAG laser (near Gaussian) and the longitudinal pump geometry. A telescope in the pump beam for the second stage (4% reflection from a prism: 30 mJ) matches the pump to the seed beam diameter of 3 mm (slightly diverging beam). The dimensions of the dye cell (gain length 15 mm) are somewhat larger to avoid diffraction. Typical output powers of the second stage are 5–6 mJ. The beam then diverges further and is finally collimated to 8 mm diam. Amplification of this beam in the third stage delivers $\sim$220 mJ at 584 nm, from a pump power of 650 mJ (8 mm diam, gain length 20 mm). The bandwidth of the PDA is typically 90–95 MHz, measured using an etalon with a bandwidth of 30 MHz.

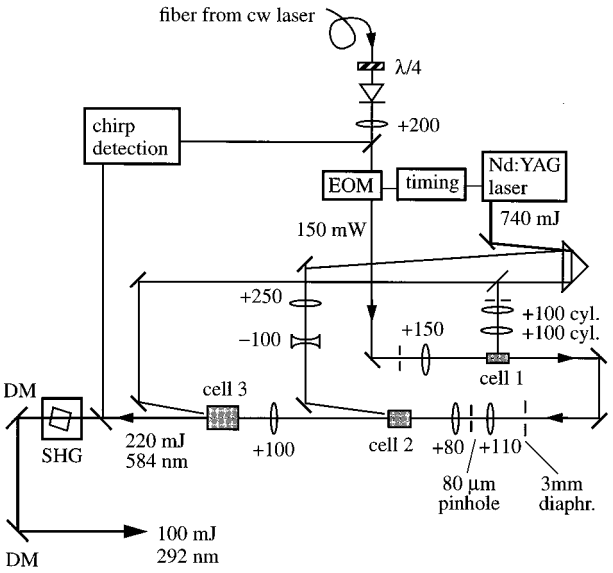

FIG. 4. The pulse dye amplifier (EOM, electro-optic modulator; DM, dichroic mirror, FI, Faraday isolator; SHG, second harmonic generation). Focal lengths of various lenses are given in mm.

The PDA output is frequency doubled in a KD*P crystal of 20 mm length to generate up to 100 mJ at 292 nm. Separation of the UV from the fundamental radiation is performed with two dichroic mirrors. When all reflection losses due to windows and crystal surfaces are taken into account, a second-harmonic conversion efficiency of 63% is estimated. This high efficiency reflects the good spatial quality and spectral purity of the PDA beam. The UV beam has a (small) divergence of $\sim$0.4 mrad. Nonoptimal phase matching then results in a slight UV beam asymmetry which is detected by two photodiodes. The difference signal of the diodes is used in a feedback loop to adjust the crystal angle. In this manner the UV power is kept optimal during the measurements with a long term stability better than 5%; pulse to pulse intensity variations are within $\sim$10%.

C. Fifth-harmonic generation and signal detection

The vacuum setup of the XUV spectrometer consists of three differentially pumped chambers. In the first chamber

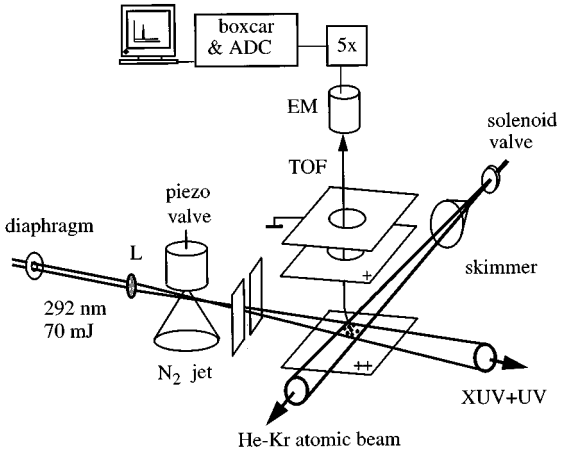

FIG. 5. The XUV spectrometer setup with ion detection. Note that the setup at the right side of the lens L is kept under vacuum (10^{-5}–10^{-7}mbar). This part consists of three differentially pumped vacuum chambers; in one XUV is generated in a N_2 jet, in a second the atomic beam is produced before entering a third interaction chamber through a skimmer (EM, electron multiplier; TOF, time-of-flight separator).

the UV is focused in a gaseous nonlinear medium for upconversion to the XUV at 58 nm. In a second chamber a pulse expansion of He generates the atomic beam. Both XUV and helium beam intersect in the third (interaction) chamber to induce the resonance transition (see Fig. 5).

Tunable radiation in the extreme ultraviolet is generated by the method of harmonic generation in a gaseous jet, which is now well established, experimentally as well as theoretically. In a perturbative approach the qth harmonic yield for a focused Gaussian beam along the z axis can be expressed as [32]

$$P_q \propto \frac{P_1^q}{(b\lambda_1)^{q-1}} N^2 |\chi_q(\omega_1,\omega_q)|^2 |b\Delta k F_q|^2. \qquad (1)$$

Here N is the density of the nonlinear medium, $\chi_q(\omega_1,\omega_q)$ is the nonlinear susceptibility of order q, and F_q is the phase-match integral over the medium with length L, given by

$$F_q = \int_{-L/2}^{L/2} \frac{e^{-ib\Delta kz/2}}{(1+iz)^{q-1}} dz, \qquad (2)$$

b is the confocal parameter of the fundamental beam, P_q and P_1 the power of the qth harmonic and fundamental radiation, respectively. The phase mismatch between the driving and generated field expressed in the wave vectors k is given by $\Delta k = k_q - qk_1$.

The nonlinear susceptibility decreases rapidly for higher-order processes. From Eq. (1) it is apparent that high UV power is the most effective way to compensate for this effect. Also a high density and resonances in the medium at the 2-, 3-, or 4-UV photon level may enhance the nonlinear susceptibility and thereby the harmonic yield by several orders of magnitude. The energy level structure of the particles in the nonlinear medium also determines whether the medium is either negatively ($\Delta k<0$) or positively dispersing ($\Delta k>0$). This is important for the phase-match integral F. In case of tight focusing ($b \gg L$) optimal phase matching for harmonic production is achieved in negatively dispersing media, while in case of positively dispersing media loose focusing ($b \gg L$) is best [33,34]. For third-harmonic generation these conditions can be met by choosing a proper mixture of gases [35]. In this case energy conversion efficiencies of typically 10^{-4} to 10^{-6} can be obtained [18].

For fifth-harmonic conversion to 58 nm the situation is quite different. Because the fifth-order nonlinear susceptibility is low, very high peak powers of the fundamental UV radiation are required. A typical focal length of 25 cm used for focusing the UV results in our case in power densities of 10^{12}–10^{13} W/cm^2. Under these conditions intermediate resonances must be avoided as they will enhance multiphoton transitions, eventually leading to ionization and optical breakdown of the medium. In Sec. III B 1 the detrimental effects of ionization on XUV production are discussed in more detail. In addition, phase matching is not easily adjusted because the XUV photon energy is well above the bound state energies of most gases (except neon and helium).

Equation (1) is in principle only valid for the low-field regime (power density $<10^{12}$ W/cm^2). When the intensity is larger than 10^{13} W/cm^2 the force of the electromagnetic field on the electrons becomes equal or even surpasses the internal forces of the atom. A perturbative approach is then no longer valid and an alternative description is required [36]. Our present situation is somewhere in between these two regimes of harmonic generation. In Sec. III B 4 high-field harmonic generation is discussed in relation to chirp-induced calibration errors.

Several gases such as Xe, C_2H_2, and N_2 were employed as nonlinear medium with backing pressures of a few bar. Although Xe is often used for third-harmonic generation because of its high nonlinear susceptibility, the low threshold for ionization and optical breakdown makes it unsuitable for fifth-harmonic generation using nanosecond pulses. Both C_2H_2 and N_2 have a lower nonlinear susceptibility, but they are more resistant to breakdown. These gases were chosen as nonlinear medium for most of the measurements as the lower susceptibility can be compensated to a large extent by a high gas density. We use a free jet as nonlinear medium (see, e.g., Ref. [20]), in which high gas density at the location of the focus is combined with high vacuum conditions along the path of XUV propagation. The pulsed jet of ~ 150 μs duration and estimated density of a few mbar is produced by a home-built, piezoelectrically driven valve after a design of Proch and Trickl [37]. A diffusion pump with liquid-nitrogen baffle is used to maintain an average background pressure of $\sim 2\times 10^{-5}$ mbar. Higher background pressures result in reabsorption of the XUV because of the high photon energy, well above the ionization threshold of most gases. Approximately 10^6 photons at 58 nm are produced per laser pulse (see below). Third-harmonic radiation at 97 nm is produced simultaneously at much higher intensities, but this does not affect the experiment as helium is transparent at this wavelength. The XUV and UV pulses overlap both spatially and in time. Both beams pass through a 3 mm hole and a variable slit diaphragm into the interaction chamber where the $1\,^1S$-$2\,^1P$ transition is induced. The slit was used to determine the divergence of the fifth-harmonic beam which turns out to be approximately $\frac{1}{4}$ of the UV beam divergence. The

UV divergence and power density in the interaction region depend on the focal length of the lens used to focus the UV for fifth-harmonic conversion. This dependence was used to determine the influence of the dynamic Stark effect induced by the high UV power density on the helium energy level structure. This is described in Sec. III C. For the $f=24.3$ cm lens used in the final Lamb shift measurement the XUV divergence is ~ 18 mrad, resulting in a power density on the order of 100 mW/cm^2 at 58 nm in the interaction region.

To reduce Doppler effects, the $1\,^1S$-$2\,^1P$ transition is induced in a helium atomic beam produced in a differentially pumped chamber by a pulsed (supersonic) expansion. Both pure He and a 10–90% He/Kr mixture were used. The backing pressure is typically 3 bar for the solenoid valve (General Valve) generating the pulsed expansion. The average pressure in this source chamber is kept below 2×10^{-5} mbar by a 2500 l/s diffusion pump. A skimmer is used to select the central part of the expansion, thereby reducing the beam divergence considerably. Further details of this skimmer and other methods to reduce Doppler effects are discussed in Sec. III A.

In the interaction chamber, kept at pressures below 5×10^{-7} mbar by a turbomolecular pump, the XUV/UV and helium beams perpendicularly intersect. Once the XUV induces the transition to the short lived $2\,^1P$ level (0.556 ns [38,39]) the powerful UV ionizes the excited atoms. High UV power (>10 MW/cm^2) is necessary to compete with the fluorescence decay back to the ground state (see Fig. 1). The high UV power density also gives rise to dynamic Stark shifts in helium (Sec. III C) and fragmentation of hydrocarbons from pump oil into many ionic fragments. For the dynamic Stark shift measurements at high UV power a liquid nitrogen cold finger was used to reduce the amount of pump-oil fragments.

A delayed and pulsed electric field of ~ 50 V/cm is used to extract the ions into a time-of-flight tube to separate the masses of ^{3}He, ^{4}He, and unwanted pump-oil fragments. Detection is performed using an electron multiplier. Pulse-to-pulse signal fluctuations of $\sim 50\%$ were observed. After amplification the signal is stored on a computer (SUN 4) using a BOXCAR integrator and a 12 bit AD converter interface (Stanford Research Systems SR250 and SR245, respectively). A measurement is performed by computerized scanning of the cw ring laser in small steps. For each step the ion signal of four laser pulses is averaged. The absolute frequency position is recorded on-line using the 150 MHz etalon and saturation spectroscopy in I_2 as described in Sec. II A.

The fifth-harmonic yield is derived from the number of He ions detected, taking into account absorption, ionization, and detection efficiency. For the He/Kr mixture using the 24.3 cm UV focusing lens typically a few hundred ions per laser pulse were detected. Using pure helium the ion signal saturated because of total absorption of XUV at a more than an order of magnitude increased signal. From this it may be concluded that the absorption in the He/Kr mixture is of the order of a few percent. Due to the short lifetime (0.56 ns) of $2\,^1P$ only a few percent of all atoms that absorb an XUV photon are ionized. Combined with a detector efficiency of $\sim 30\%$ a minimum XUV yield at 58 nm of $\sim 10^6$ photons per laser pulse is estimated. This corresponds to a power density on the order of 100 mW/cm^2 in the interaction region, far below the saturation intensity of 190 W/cm^2 for the $1\,^1S$-$2\,^1P$ transition. Although the transition is not saturated, broadening effects were observed of the order of 10–20 % of the linewidth due to saturation in the electron multiplier for higher He and N_2 density. The XUV bandwidth cannot be determined easily from the transition linewidth of typically 600–650 MHz due to Doppler broadening effects. However, from the chirp measurements and calculated effect on the resonance position (Sec. III B 2) an XUV bandwidth of 250 MHz can be estimated.

The UV power dependence of the He^+ signal was measured by varying the UV down to $\sim 65\%$ of the maximum. For C_2H_2 and N_2 as nonlinear media a UV dependence (ion signal $\sim P_{\mathrm{UV}}^{\kappa}$) of, respectively, $\kappa=5.0$ and $\kappa=5.5$ was found with an uncertainty of about 0.5. A power law of 6 is expected based on the fifth-harmonic process and the (unsaturated) ionization step. For N_2 a XUV power dependence on UV of 4.5 (5.5 minus one for ionization) is obtained, which was used in calculating the effect of chirp on the $1\,^1S$-$2\,^1P$ transition (Sec. III B).

III. SYSTEMATIC EFFECTS

Although calibration can be accurately performed in the visible due to the frequency relation $f_{\mathrm{XUV}}=10f_{\mathrm{vis}}$, several systematic error sources are important for a precise determination of the $1\,^1S$-$2\,^1P$ transition frequency. In this respect it is an advantage that the harmonic up-conversion to 58 nm is not enhanced by intermediate resonances in the nonlinear medium, which implies that the fifth-harmonic yield does not strongly depend on wavelength. Therefore no distortion or shift of the transition line shape is expected. Three other phenomena, Doppler shift, frequency chirp, and dynamic Stark shift, do have a significant effect of several tens of MHz on the calibration. Each error source will be discussed separately in the following sections, including extensions to the setup needed to measure and control the effects.

A. Doppler effects

The one-photon $1\,^1S$-$2\,^1P$ transition is highly sensitive to Doppler shifts and broadening. To reduce these effects a geometry with perpendicularly crossed and collimated beams is chosen (see also Figs. 2 and 5). The average velocity of pure helium in the pulsed expansion is 1200(300) m/s, deduced by comparing the flight time of the helium atoms for various distances between the nozzle and interaction zone. An expansion of 10% He in 90% Kr reduces this velocity to 480(100) m/s due to He-Kr collisions in the first few cm of the expansion [40]. No significant difference in velocity (''velocity slip'') between ^{3}He and ^{4}He occurs because of the small mass difference compared to the mass of Kr. Consequently the Doppler shift in a pure He beam is 2.5 times larger than in a He/Kr beam. This difference is used to align the XUV/UV and helium beams perpendicularly. As long as a Doppler shift exists, the He/Kr and pure He will show a difference in transition frequency. The geometrical beam alignment is adjusted until this difference is comparable to the statistical uncertainty in this measurement. A possible source for a Doppler shift of several MHz induced by asymmetry of absorption in the atomic beam is minimized by

taking equal partial helium pressures for the pure He and the He/Kr beam during the alignment procedure.

Doppler broadening of the transition is related to the divergence of the atomic beam and to the velocity spread of the atoms. The XUV divergence is generally a few times smaller and therefore only marginally contributes to broadening. In principle the divergence of the helium beam depends on the geometry, determined by the diameters and positions of skimmer and nozzle openings. However, backscattered atoms from the skimmer can disturb the beam, resulting in an increased divergence. Without Doppler effects a *symmetric* linewidth of ~400 MHz is expected, based on the linewidth of our XUV source of ~250 MHz (see Sec. II C) and natural linewidth of 286 MHz. Any broadening beyond 400 MHz is interpreted as Doppler-induced. In the earlier experiments, including the determination of the isotope shift [23], a metal skimmer (90° total cone angle and orifice of 2 mm) was used. Although from geometrical considerations a 500–600 MHz linewidth was expected, both isotopes showed the same asymmetric line shape with a width of 950 MHz for pure He as well as for the He/Kr mixture. In spite of this peculiar behavior, the Doppler shift depended on the XUV atomic beam angle as predicted. This was an indication that the 90° skimmer diffused the atoms, although the beam direction was still determined by the skimmer-nozzle axis. As no significant differences for the line shapes for ^{3}He and ^{4}He were found, the resulting uncertainty in the isotope shift due to shape and related effects was limited to only 3 MHz.

However, the absolute transition frequency in that measurement was severely hampered by asymmetric line shapes, resulting in an uncertainty contribution of 70 MHz [23]. A test was performed to study this effect with a 3 mm wide slit mask in the ion collection system along the direction of the helium beam. The skimmer was mounted at a distance of about 20 cm from the interaction region, with a skimmer-nozzle distance of 15 cm. The slit selected a small part of the helium beam contributing to the signal. In this case the line shape became symmetric with a linewidth reduction to 500(30) MHz. This is the narrowest linewidth observed, but the use of a slit is not practical for the beam-alignment procedure described earlier in this section. Therefore a new skimmer was designed by deforming acrylic sheet plastic. This skimmer is steep (total cone angle $<15°$) and ''volcano shaped,'' smooth, thin (0.1 mm), and has an opening of 2.5 mm diam. With this skimmer a minimum linewidth of ~600 MHz and a symmetric profile for the $1\,^1S$-$2\,^1P$ transition is obtained. Pure helium gives a symmetric linewidth of ~850 MHz and a line shape resembling more a Lorentzian than a Gaussian. From these line shapes and widths it can be concluded that the Doppler broadening for the He/Kr mixture is best described by convolution with a 200 MHz FWHM Lorentzian.

B. Frequency chirp

When a laser beam experiences a time-dependent refractive index, its optical phase is modulated by an amount equal to $\Phi(z,t)$. The resulting time-dependent frequency deviations Δf (chirp) from the original frequency f can be expressed as

$$\Delta f(t)=\frac{1}{2\pi}\frac{d\Phi}{dt}. \tag{3}$$

Sources for this effect are self-phase modulation (optical Kerr effect), time-dependent ionization of the medium of propagation (in nonlinear up-conversion processes [41]), and time-dependent gain (in PDA's).

In this section chirp occurring in pulse amplification of a cw seed frequency is considered as it has the largest impact on the calibration of the present Lamb shift measurement. Due to the harmonic up-conversion process any frequency deviation from the seed laser in the visible results in a frequency excursion ten times as large in the XUV. Frequency chirp in a PDA has recently been the subject of several investigations [24,25,42], from which it is now well established that the origin of chirp in a PDA is time-dependent gain in the amplification process. This can be explained using the Kramers-Kronig relations [43], connecting the absorption (i.e., negative gain) to the refractive index of a material. Melikechi *et al.* [25] have shown that one may write

$$\Delta f(z,\tau)=\frac{\alpha_0(\omega)-\alpha_1(\omega)}{2\lambda n_s(\omega)}\frac{d}{d\tau}\left[\int_0^z N_1(z,\tau)dz\right]. \tag{4}$$

Here $\omega=2\pi f, \tau=t-zn_s(\omega)/c$ is the time coordinate transformed to the moving pulse window, n_s is the refractive index of the dye solvent, and N_1 the excited state population of the dye, which is a function of time τ and position z along the beam direction in the amplifier cell. The two coefficients α_0 and α_1 in Eq. (4) can be calculated from the absorption cross section $\sigma_0(\omega)$ and the fluorescence cross section $\sigma_1(\omega)$, respectively, as given by Haas and Rotter [44]:

$$\alpha_i(\omega)=-2cn_s(\omega)\mathrm{P}\int_0^\infty\left[\frac{\sigma_i(\omega')}{\pi(\omega'^2-\omega^2)}\right]d\omega', \tag{5}$$

where P denotes the principal integral. When the absorption and fluorescence band of a dye are well separated, α_0 is negligible due to the frequency denominator in Eq. (5). It follows that there must be a wavelength in the fluorescence band where α_1 is zero [due to the denominator in Eq. (5)], leading to chirp-free amplification. Such behavior has been demonstrated in DCM dye at 661.95 nm by Melikechi *et al.* [25]. Often the combination of wavelength and dye cannot be chosen freely, and the absorption and fluorescence band may overlap such as for the Rhodamine B dye used in the present experiment. Frequency chirp is therefore inevitable in many experiments with a PDA.

A solution is to eliminate chirp actively by applying a counteracting phase modulation with an electro-optic modulator (EOM) on the seed beam of the PDA. This technique was investigated independently by Reinhard *et al.* [45] for measurements on muonium using PDA pulses of ~20 ns duration. Due to the nanosecond time scale of the pulses (in the present case 6.5 ns) this compensation cannot be tailored for each individual pulse. However, the average chirp over multiple pulses can be reduced considerably, as demonstrated in Sec. IV.

When chirp and intensity profile of the XUV pulse can be measured, it is possible to calculate the effect on the $1\,^1S$-$2\,^1P$ resonance frequency. The difficulty is that the

XUV intensity profile has to be measured with subnanosecond resolution, which is a technical problem. To investigate the net effect of chirp in the PDA on the resonance frequency, several detailed measurements have been performed where the chirp was actively increased (''extra-chirp'') and decreased (''antichirp'') with the use of an EOM in the seed-laser beam (see the next section). When the EOM is not used, the chirp in the PDA is referred to as ''normal chirp.''

1. Chirp measurement and modification procedure

The chirp measurement principle used is similar to that described by Fee *et al.* [24] and Ganghopadhyay [42]. It is based on heterodyning the cw seed laser with the pulsed output of the PDA. The total beat intensity $I_b(t)$ is

$$I_b(t)=I_p(t)+I_{\mathrm{cw}}+2\sqrt{I_p(t)I_{\mathrm{cw}}}\frac{e^{i\Phi(t)}+e^{-i\Phi(t)}}{2}. \qquad (6)$$

I_p and I_{cw} are the PDA and cw laser intensities, respectively. A small part of the PDA beam is selected for this measurement ensuring that the beat signal is not averaged out due to spatial interference patterns. The initial phase difference depends on the path difference and therefore varies from pulse to pulse. For this reason averaging of the beat wave is not possible and the chirp analysis algorithm has to be used for each pulse separately. To reconstruct the difference phase $\Phi(t)$ a Fourier-transform-filtering (FFT) technique is applied as demonstrated by Fee *et al.* [24]. It requires that the reference beam is frequency shifted by an amount f_m. When $\Delta f \ll f_m$ the heterodyne (difference) phase is approximately equal to

$$\Phi(t)=2\pi\int_t[\Delta f(t')+f_m]dt'\approx 2\pi f_m t. \qquad (7)$$

Insertion of Eq. (7) in Eq. (6) shows how to reconstruct the phase. Retaining only the positive (or negative) frequency components in the FFT of $I_b(t)$ one of the exponentials in the beat signal is selected from which the phase is easily retrieved. This method requires that the frequency components associated with the pulsed envelope (I_p) are well separated from the true heterodyne signal. For the $\sim$20 ns long pulses in Refs. [24,42] this is accomplished by frequency shifting the cw laser a few hundred MHz with an acousto-optic modulator (AOM). A bandpass filter can then be used to select the pulse-independent heterodyne signal. The short PDA pulses of 6.5 ns duration in our experiment would require an awkwardly high offset frequency of $\sim$1 GHz and a detection bandwidth of several GHz to obtain an accuracy better than 1 MHz. Instead, we measure the pulsed intensity profile I_p in such a way that it can be eliminated from I_b with high accuracy. Reconstruction of the phase with the FFT-filtering method can in this way be performed with a low offset frequency of 250 MHz.

In Fig. 6 a schematic of the chirp measurement and phase modification setup is shown. Part of the output of the seed beam (10 mW) is split off to serve as a phase reference, 250 MHz shifted by an AOM (accuracy 1 kHz). The main seed beam travels through a pulsed EOM which allows for modification of the input phase before amplification in the PDA. Part of the output of the PDA is recombined with the

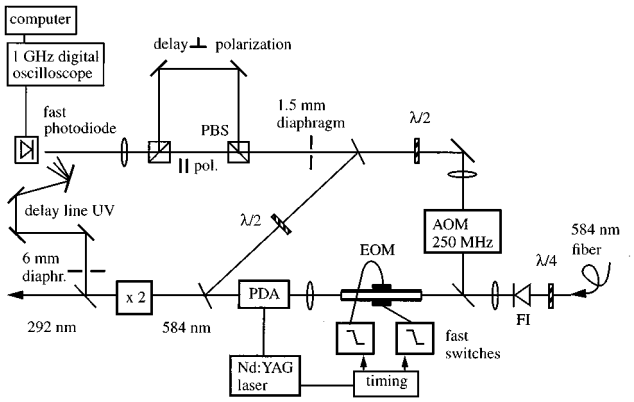

FIG. 6. Chirp detection and modification setup (AOM, acousto-optic modulator; PDA, pulse-dye amplifier; EOM, electro-optic modulator; FI, Faraday isolator; PBS, polarizing beam splitter).

frequency-shifted seed beam on a quartz plate to generate a heterodyne beat signal. A diaphragm of 1.5 mm diam, which can be displaced transversely to measure the position dependence of chirp, selects a small part of the PDA beam. The intensity in the beam profile is not a fixed function of position due to random fluctuations induced by the pump laser (sometimes mode-beating effects are observed) and by Schlieren effects in the dye. To be able to divide out the pulse envelope it is therefore necessary to measure the pulse at the same spot where the heterodyne signal is observed. For this purpose two half-wave plates are used to obtain a cw laser beam with pure linearly (horizontal) polarized light, and a PDA beam with both linear polarization components. The parallel components generate the beat signal, while the perpendicular polarization component of the PDA output is unaffected by the cw light. Both signals are recorded on the same photodiode, separated in time by a polarization-dependent delay line of $\sim$25 ns. This ensures that also the electronic detection properties are the same. Once the delay and the amplitude ratio of the pulse component in both signals have been calibrated (cw light off) the pulse envelope can be subtracted and divided out from the signal I_b. To calculate the effect of chirp on the resonance transition also the UV intensity profile is measured on the same photodiode (delay $\sim$50 ns). As the photodiode is not sensitive at 292 nm, the fluorescence of a piece of black felt is measured instead. Due to the short fluorescence time of this material ($<$1 ns) the UV pulse profile is not significantly broadened. The total bandwidth of the 1 GHz photodiode combined with the 1 GHz, 5 Gs/s, 8-bit digital oscilloscope (Tektronix TDS680B) is $\sim$800 MHz, which was determined by measuring the response of laser pulses of 100 fs duration.

In Fig. 7 the different stages of the chirp measurement procedure are shown. Part (a) of Fig. 7 shows a typical oscilloscope readout. Electrical and digitizing noise limit correction with the measured pulse intensity to the central part of the heterodyne signal with a pulse component larger than 10% of the maximum intensity. Outside these regions the pulse corrected beat signal is extrapolated with a slowly decreasing sinusoidal [Fig. 7(b)]. In this way wraparound effects are avoided in the FFT of this signal. Only the positive frequency components are transformed back (high-frequency noise components are filtered out as well), from which the

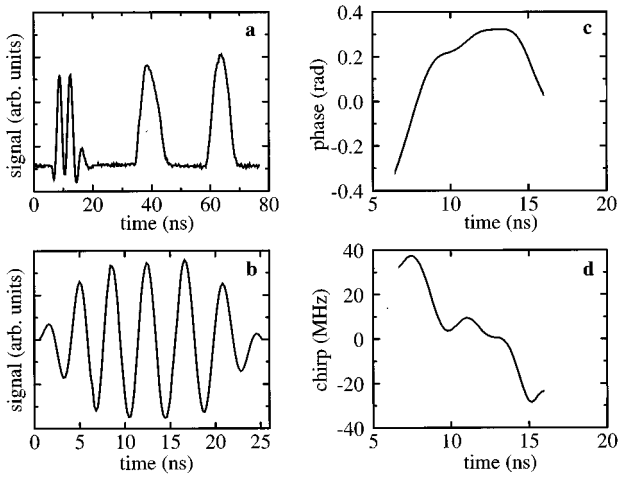

FIG. 7. Chirp measurement and analysis procedure of a single laser pulse (*a*, typical oscilloscope readout, with the beat signal between the PDA output and the 250 MHz frequency shifted cw beam, the PDA pulse, and UV pulse; *b*, pulse corrected and extrapolated heterodyne signal; *c*, reconstructed phase; *d*, calculated chirp).

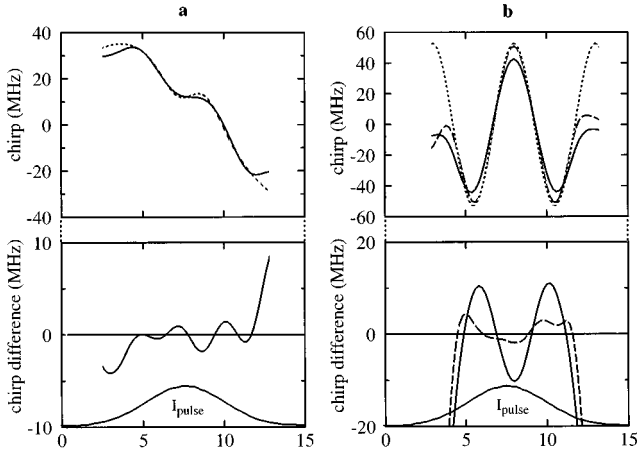

FIG. 8. Comparison between simulated (dotted lines) and reconstructed chirp (solid and long-dashed line); in the lower part the difference between simulated and reconstructed chirp is given, together with the simulated pulse intensity. Part *a*, reconstruction of ''normal'' chirp. Part *b*, reconstruction of extra strong chirp using the standard method (solid line) and the line arized heterodyne signal method (long-dashed line). See text for description of chirp reconstruction methods.

difference with the AOM frequency can be determined. In part(c) of Fig. 7 the resulting phase evolution is shown. The initial phase depends on the optical path difference of cw and PDA beam which is different for each pulse. Using Eq. (3) the frequency chirp is calculated from the measured phase as shown in part (d) of Fig. 7. Pulse-to-pulse fluctuations in the chirp are typically on the order of 5–10 MHz. To reduce the effect of these real and detection-noise-induced fluctuations most chirp measurements were averaged over 50–100 laser pulses.

The total chirp measurement process has been automated and the chirp of one out of every three laser pulses is determined (limited by computer and data transfer time of the oscilloscope). In addition an estimate for the XUV shift is calculated from each measurement based on weighting the chirp with the 5.5th UV power dependence of the ionization signal (Sec. II C).

To estimate the accuracy of the chirp measurement procedure extensive computer simulations were performed, including noise and other typical experimental features. From simulations [Fig. 8(a)] of normal chirp variation of <10 MHz/ns within the pulse it can be concluded that the reconstruction algorithm predicts the chirp for a large part of the pulse very well. For the PDA pulse time window with an intensity larger than 40% of the maximum, deviations of $\sim 1-2$ MHz from the simulated chirp are found with a tendency to ''cut corners'' for rapid chirp variations. In the leading and trailing part deviations increasing up to ~ 10 MHz are observed, attributed to the extrapolation of the heterodyne signal to decrease the effect of noise. The net effect on the XUV measurement is on average calculated (Sec. III B 2) to be smaller than a few MHz due to the averaging over the expected ion signal. The total calculated chirp-induced shift of the resonance (average over 50 laser pulses) shows random fluctuations of typically 5 MHz. Based on simulations and measurements an uncertainty in the XUV measurements of 10 MHz due to the chirp measurement procedure is estimated. The uncertainty in the actual XUV intensity function introduces an additional uncertainty in the net effect of chirp as discussed in Sec. IV B.

Because of the good transverse beam profile of the PDA the variation of the chirp is typically 1–2 MHz over its central part (5 mm out of 8 mm total beam diameter), and up to 4–5 MHz outside this region. This was measured with the 1.5 mm diaphragm in the PDA beam. To reduce the uncertainty in the absolute transition measurement only the central 5 mm ($\sim 70\%$ of the total power) of the PDA output was used for harmonic up-conversion during the Lamb-shift measurement. The uncertainty in the XUV resonance frequency due to spatial variation of chirp is estimated to be ~ 20 MHz.

The chirp and phase are monitored continuously and phase adjustments with the pulsed EOM are performed interactively to either increase or decrease the chirp of the PDA. The EOM consists of a $20\times 0.5\times 0.6$ mm $LiTaO_3$ crystal driven on each side with a fast voltage switch (range 0–30 V). The risetime is adjustable from 1.5 ns to 10 ns, and a delay of both pulses can be set independently relative to the Nd:YAG laser pulse (delay generator: Stanford Research Systems DG535); Nd:YAG laser pulse timing jitter is ± 0.6ns. Decreasing chirp with the EOM by applying a counteracting phase modulation reduces the sensitivity of the calculated effect on the XUV production function. This is used to perform highly accurate ''antichirped'' measurements. By introducing an extra large chirp pulse of ~ 80 MHz in 2 ns the transition linewidth and shape is made sensitive to the effective XUV production time dependence, which can thus be investigated accurately. Simulations of such strong extra chirp, however, show that the approximation in Eq. (7) is then no longer valid, and can lead to an underestimation of the chirp amplitude by as much as 20–30%. We found that the reconstruction algorithm can be improved in this case, by reducing the number of frequency components in the heterodyne signal in a recursive manner. For this purpose the reconstructed phase is used to linearize and resample the het-

erodyne signal. This procedure is then repeated two times and the total phase is obtained by adding the results of all intermediate steps. Figure 8(b) shows the improvements using such a procedure. Although still slightly underestimated, large chirps are measured more accurately in this way, leading to a better agreement between calculated and measured line shapes (see Sec. IV).

2. Line shape calculations

To have an indication of the influence of chirp on the $1\,^1S$-$2\,^1P$ transition during the measurements, an estimate of the ion-signal intensity weighting over the measured chirp is used to calculate the chirp-induced shifts. However, for a correct description the coherent nature of the excitation process has to be considered. The final analysis is based on the density matrix formalism (see, e.g., Boyd [46]).

As shown in Fig. 1, the excitation scheme is similar to a two-level system in which ω (linearly polarized XUV) couples the $1\,^1S$ and the $2\,^1P$ state (difference frequency ω_{12}) via a dipole interaction V. Fluorescence back to the ground state at a rate Γ induces the largest damping (fluorescence to $2\,^1S$ is 10^{-3} times weaker and therefore negligible). The effect of the ionizing UV intensity I_{UV} is incorporated into the equations of motion by introduction of a dynamic Stark shift $\Delta_s=\beta I_{\mathrm{UV}}$ and an ionization rate $\eta=\sigma I_{\mathrm{UV}}$ [46]. The dynamic Stark constant β and ionization cross section σ are discussed in Sec. III C. Without explicitly showing the time and position dependences of η, V, and the density matrix elements ρ, the equations of motion can be written as

$$\frac{d\rho_{21}}{dt}=\frac{d\rho_{12}^*}{dt}=-\left\{i(\omega_{12}+\Delta_s)+\frac{\Gamma+\eta}{2}\right\}\rho_{21}+\frac{i}{\hbar}V_{21}(\rho_{22}-\rho_{11}), \tag{8}$$

$$\frac{d\rho_{11}}{dt}=\Gamma\rho_{22}+\frac{i}{\hbar}(V_{21}\rho_{12}-\rho_{21}V_{12}), \tag{9}$$

$$\frac{d\rho_{22}}{dt}=-(\Gamma+\eta)\rho_{22}-\frac{i}{\hbar}(V_{21}\rho_{12}-\rho_{21}V_{12}), \tag{10}$$

$$\frac{d\rho_{33}}{dt}=\eta\rho_{22}. \tag{11}$$

Here ρ_{11}, ρ_{22}, and ρ_{33} represent the populations of the ground, excited, and ionic state, respectively. The interaction V is given by

$$V_{12}=V_{21}=\frac{\mu_{12}E_0}{2}(e^{i\omega t}+e^{-i\omega t}) \tag{12}$$

with $\mu_{12}=er_{12}$ the transition dipole moment. Substitution of

$$\rho_{21}=\rho_{12}^*=e^{-i\omega t}\tilde{\rho}_{21}=e^{-i\omega t}(\tilde{\rho}_{21}^r+i\tilde{\rho}_{21}^i) \tag{13}$$

together with the rotating wave approximation [46] removes the optical frequencies from the coupled differential equations (8)–(11), resulting in

$$\frac{d\tilde{\rho}_{21}}{dt}=-\left(i(\omega_{12}+\Delta-\omega)+\frac{\Gamma+\eta}{2}\right)\tilde{\rho}_{21}+\frac{i}{2\hbar}\mu_{12}E_0(\rho_{22}-\rho_{11}), \tag{14}$$

$$\frac{d\rho_{11}}{dt}=\Gamma\rho_{22}+\frac{1}{\hbar}\mu_{12}E_0\tilde{\rho}_{21}^i, \tag{15}$$

$$\frac{d\rho_{22}}{dt}=-(\Gamma+\eta)\rho_{22}-\frac{1}{\hbar}\mu_{12}E_0\tilde{\rho}_{21}^i, \tag{16}$$

$$\frac{d\rho_{33}}{dt}=\eta\rho_{22}. \tag{17}$$

The experimentally observed signal is proportional to ρ_{33}. The $1\,^1S$-$2\,^1P$ dipole moment and fluorescence rate are $\mu_z=3.56\times10^{-30}$ C m and 1.8×10^9 s^{-1}, respectively [38]. The ionization cross section σ at 292 nm is 4.1×10^{-18} cm^2 [47] (for linear polarization, $\Delta m=0$). To integrate Eqs. (14)–(17) the UV and XUV frequency and intensity functions deduced from chirp measurements are used as input. The time-dependent XUV field amplitude E_0 is approximated by (see Sec. II C)

$$E_0=\zeta\left(\frac{2I_{uv}^{\kappa}}{\varepsilon_0 c}\right)^{1/2}. \tag{18}$$

Here ζ is a scaling constant to match the field strength to the estimated XUV yield. As N_2 was used as a nonlinear medium for fifth-harmonic generation we used $\kappa=4.5(0.5)$ (Sec. II C) for all calculations of the line shape. The coupled differential equations (14)–(17) have been integrated with the Burlisch-Stoer method (adaptive stepsize) [48] for the UV and XUV intensities in the center of the XUV beam, as a function of frequency. For this purpose the excitation probability was calculated for 100 frequency points evenly distributed over an interval of 4 GHz around the transition frequency. Cubic-spline interpolation was used in between these points. Without Doppler broadening a linewidth of $\sim$400 MHz (natural linewidth 286 MHz) is found using typical experimental chirp and UV pulse data. Doppler broadening is included by convolution with a 200 MHz Lorenzian (see Sec. III A).

3. Chirp properties of the PDA

The observed wavelength dependence of chirp in the PDA with all three amplifiers active is quite strong as shown in Fig. 9. Probably due to the overlapping fluorescence and absorption band of Rhodamine B, the chirp is never close to zero. On the short wavelength side, closer to the absorption band of Rhodamine B, the phase at the end of the pulse does not return to its original starting point. An explanation might be that at the short wavelength side the amplified beam is reabsorbed, keeping the excited state population high instead of decreasing it. Despite the strong wavelength dependence of the chirp, its effect on the isotope shift can be neglected due to the small frequency separation of only 1 cm^{-1} in the visible between the ^{3}He and ^{4}He resonance lines.

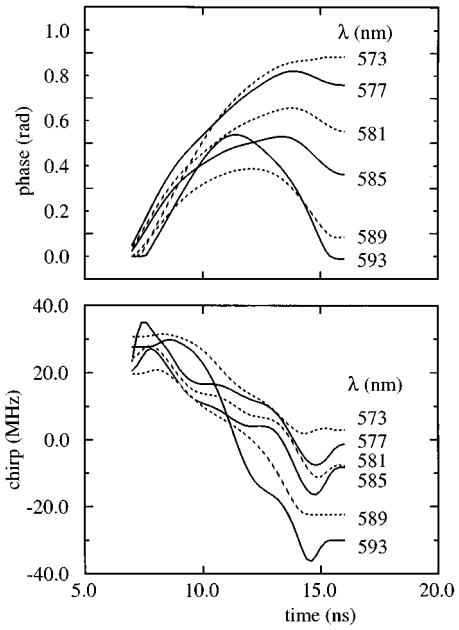

FIG. 9. Observed wavelength dependence of phase evolution and reconstructed chirp in the PDA (average 50 laser pulses, all amplifier stages Rhodamine B dye).

In contrast to what might be expected from Eq. (4), the strongest chirp effects were seen for the lowest pump power in the first amplifier cell. The reason probably is saturation of the gain for high pump power, which reduces the phase modulation during the pulse amplification. A similar effect is seen when the second and third amplifier stages are added. The chirp decreased with each extra amplifier, instead of an increase as observed by Fee *et al.* [24]. Changing the seed power from 30 to 150 mW made no significant difference for most of the PDA pulse. Only in the leading and trailing edge were deviations of the order of 5 MHz observed.

From the measurements it is clear that chirp cannot be neglected in these XUV experiments. For this reason the phase modulation in the PDA is actively altered with an EOM as described in Sec. III B 1. The results of induced extra- and antichirp on the calibration will be presented together with final measurements in Sec. IV.

4. Chirp in frequency doubling and harmonic generation

Measuring chirp induced in a frequency-doubling process is difficult [42] and can lead to erroneous conclusions about the amplitude and even the sign of the chirp [49]. Therefore recent realistic calculations of chirp in frequency doubling in a KDP crystal by Smith and Bowers [49] were used; they included strong fundamental power depletion (conversion efficiency 56%), diffraction, absorption, and beam walkoff. One of their main conclusions is that no significant phase modulation is induced in the doubled light under conditions of perfect phase matching in combination with negligible losses due to absorption, diffraction, or beam walkoff. However, any deviation from this ideal situation, such as a sizeable phase mismatch, will result in frequency chirp. Diffraction and beam walkoff are not important in the present situation because of the large beam diameter of 8 mm. We expect chirp mainly because of a possible phase mismatch. A phase mismatch Δk of maximally 0.07 mm^{-1} is estimated for our 20 mm long KD*P doubling crystal. This is based on an estimated maximum efficiency reduction of 15% due to imperfect feedback and an effective beam divergence of ~ 0.4 mrad. As the ion signal strongly depends on UV power, the lower yield for mismatched UV production helps to reduce the net effect of mismatch-induced chirp.

The chirp is roughly proportional to phase mismatch and laser power. Translating the results in Ref. [49] to the visible power density of ~ 70 MW/cm^2 and a maximum phase mismatch in our crystal results in a phase modulation of at most 30 mrad. For 6 ns UV pulses this corresponds to frequency excursions ranging from $+1.6$ MHz to -1.6 MHz in the UV. Simulations using typical experimental data for the UV/XUV intensity profiles show that the net shift is negligible (-0.4MHz). The reason is that the chirp largely averages out, especially because XUV production only takes place close to the maximum of the UV power where the chirp (not the phase) changes sign.

In this discussion the optical Kerr effect in KD*P has been neglected because of its small magnitude. From the nonlinear refractive index in the visible of $\sim 6\times 10^{-16}$ cm^2/W [50] a phase modulation of only -0.9 mrad is calculated. The nonlinear refractive index at 292 nm is of almost equal size, but with opposite sign [50,51], resulting in an even lower, and negligible chirp amplitude.

At the UV power densities used for fifth-harmonic generation (10^{12}–10^{13} W/cm^2) frequency chirp may arise from ionization and/or excitation of the gaseous nonlinear medium or the optical Kerr effect. A quite large reduction of the refractive index may occur [41] when electrons created by direct ionization gain energy in the light field by an inverse ''bremsstrahlung'' process thereby ionizing other atoms and eventually resulting in breakdown of the medium. We observed strong effects of breakdown in the case of xenon as nonlinear medium. In Fig. 10 the resonance transition is shown to shift and broaden when strong breakdown in Xe is induced. An apparent downward shift of the resonance frequency as large as 400 MHz was observed (the XUV frequency shifts upward due to ionization).

These effects depend on the density of the nonlinear medium. Therefore the harmonic chirp in N_2 was determined by measuring the $1\,^1S$-$2\,^1P$ transition for different N_2 densities. At the UV power density used in the final measurements a total shift of 17 MHz was found when the density of N_2 was changed from ~ 0.5 to ~ 2 times the standard density. Linear regression to zero pressure results in a correction for the final measurements of $+10(13)$ MHz (see Table I). The error includes the uncertainty in the actual functional dependence of this chirp on N_2 density. Although this correction is on the edge of being statistically significant, such a shift can be expected based on the clear shift of 56(11) MHz (again changing the N_2 density over a factor of 4) found for doubled UV power density resulting from the use of a 1.5x telescope in the UV beam.

For progressively higher fundamental power another source of chirp becomes important, as shown recently in a number of papers on high-harmonic generation in the strong field regime (see, e.g., [36,52]). A perturbative approach is then no longer valid and a full quantum description must be

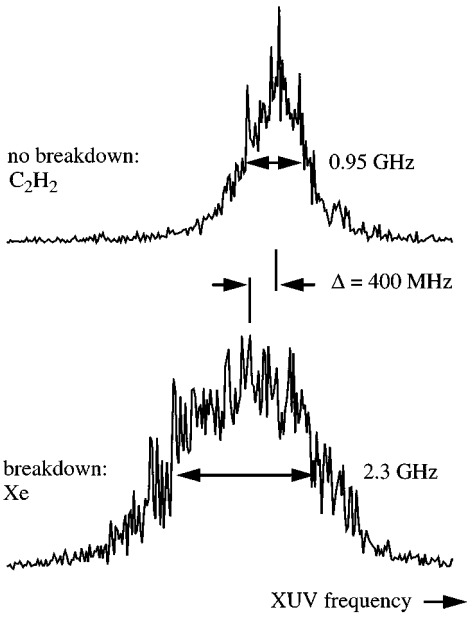

FIG. 10. Breakdown-induced broadening and shift of the He resonance position using (a) C_2H_2 and (b) Xe as nonlinear medium for fifth-harmonic conversion. Both recordings were measured with the 90° cone angle skimmer resulting in a slightly asymmetric line profile with a width of ~950 MHz even without breakdown.

used, in which the trajectory of an electron excited by the electromagnetic field is evaluated. Rapid changes in field amplitude as in short laser pulses may lead to significant chirp in the generated harmonics. Essentially a single atom effect occurs, which can have strong implications for the phase matching and propagation of the generated harmonic radiation [53,54]. As a result this chirp cannot be quantified by changing the density of the nonlinear medium. An order of magnitude estimate can be made for fifth-harmonic generation at a typical power level of 10^{12}–10^{13} W/cm^2 and pulse length of a few ns. The influence of this chirp on the transition frequency averages out to a negligible effect.

C. Dynamic Stark shift and hyperfine structure

1. Measurement of dynamic Stark shift in ^4He

High UV power (>10 MW/cm^2) is required to ionize the short-lived $2\,^1P$ state, resulting in a dynamic Stark effect induced downward shift for the ground state and an upward shift for the $2\,^1P$ level, thereby increasing the resonance frequency. The intensity of the XUV is negligible in this respect. Simply changing the UV power to measure this effect is not feasible due to the strong dependence of XUV yield on UV power. However, the $1\,^1S$-$2\,^1P$ transition is measured in quick succession with three different prealigned lenses used to focus the UV for harmonic generation (24.3 cm, 33.9 cm, and 49.0 cm). This procedure changes the UV power density in the detection region from ~16.2 MW/cm^2 for the 24.3 cm lens to ~65.9 MW/cm^2 for the 49.0 cm lens. Surprisingly, the helium signal then varies only 30%, in spite of a change in power at the focus by a factor 4. This behavior suggests a phase mismatch $b\Delta k \geqslant 0$ in the up-conversion process which is more efficient in case of loose focusing.

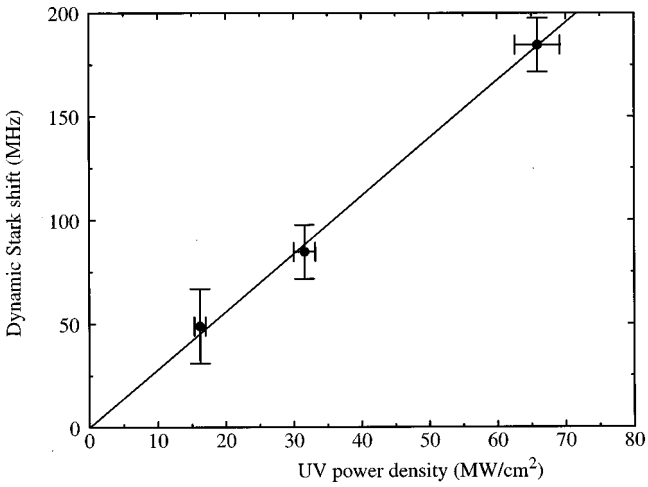

FIG. 11. Dynamic Stark shift measurement in ^{4}He as a function of the UV power density in the interaction region. The horizontal error bars indicate the uncertainty in the relative UV power densities. The absolute UV power has an accuracy of only 40–50 % (see Sec. III B).

Also higher UV power in the interaction zone helps to increase the ionization rate. Relative UV power densities in the interaction zone were determined from the focal lengths and are accurate to ~5% (including power meter reading); the absolute UV power density, however, has an uncertainty of 40–50 %. Since the 24.3 cm lens was used for the final measurements under the same conditions (power, beam profile) as in the Stark shift determination, the absolute uncertainty in the power is not important.

In Fig. 11 the results of the dynamic Stark shift measurements are shown. The vertical error bars are a combination of the statistical uncertainty of 7–9 MHz in the $1\,^1S$-$2\,^1P$ recordings and the uncertainty due to the beam alignment with the three lenses of 9–15 MHz. For the final absolute resonance position measurement a correction of $-44(15)$ MHz is found based on the shift for the 24.3 cm lens. Linear extrapolation results in a Stark shift coefficient of 2.77 Hz/W cm^2, with a conservative uncertainty of 1.3 Hz/W cm^2 almost completely due to the error in the absolute UV power density.

2. Dynamic Stark shift and hyperfine structure in ^3He

The Stark shifts in ^{4}He and ^{3}He slightly differ because of hyperfine structure in the $2\,^1P$ state of ^{3}He and the use of linearly polarized UV and XUV radiation. This difference is too small to be measured accurately. Moreover, the isotope shift is defined in the absence of hyperfine structure, which therefore must be accounted for. An extra complication is that hyperfine structure in ^{3}He ($F=\frac{3}{2}$ and $F=\frac{1}{2}$ separated by 41.63 MHz) is of the same order of magnitude as the Stark shift. So the combined effect has to be calculated before a comparison between experiment and theory for the isotope shift is possible. In the Appendix this procedure is presented in detail. The Stark shift for ^{4}He can be evaluated immediately from the dynamic scalar polarizabilities yielding a shift of 3.1(4) Hz/W cm^2, in good agreement with the value of 2.77(1.3) Hz/W cm^2 determined in Sec. III C 1. For the isotope shift measurements a UV power density of

$\sim 25\ \mathrm{MW/cm^2}$ was used [23], resulting in a shift for ^{4}He of 80 MHz. The combined shift due to the Stark effect and hyperfine structure in ^{3}He is 6 MHz lower than that of ^{4}He, with an error of 3 MHz mostly due to uncertainties in the power density. Because the transition frequency of ^{3}He is lower than ^{4}He this resulted in a correction of $-6(3)$ MHz to the measured isotope shift.

IV. RESULTS

As discussed in Sec. III several systematic effects of the same order of magnitude may influence the accuracy of the $1\,^1S$-$2\,^1P$ measurement. The dynamic Stark shift was measured in a separate experiment (Sec. III C), as UV beam quality and power were sufficiently constant for this purpose. The other two important effects, chirp and Doppler shift, were determined in combination with the final frequency calibration of the transition.

A. Extra-chirp measurements

The impact of chirp not only depends on its measurement in the visible, but also on the XUV production mechanism which in principle selects the most intense part of the light pulse. To investigate this influence a 2 ns wide additional chirp pulse of ~ 80 MHz was applied with the EOM using different time delays relative to the PDA output pulse (see also Sec. III B 1). For each time delay the $1\,^1S$-$2\,^1P$ transition line shape was determined from an average over four recordings as shown in Fig. 12. The solid lines in Fig. 12 represent the theoretical line shape calculations (Sec. III B 2) based on chirp measurements of in total 100 pulses before and after the recordings of the He-resonance line. Only the height of the calculated line shapes was fitted. The averaged chirp peaks in Fig. 12 (left side) are somewhat broader than 2 ns due to a pulse-to-pulse timing jitter of ± 0.6ns. A comparison of the experimental and calculated line shapes in Fig. 12 shows that the effect of chirp on the resonance is well understood. Some small differences are attributed to an underestimation of the chirp due to the large magnitude in this case compared to the offset frequency (Sec. III B 1).

In the analysis presented above the calculated shape of the transition is especially sensitive to the exact timing of the XUV pulse relative to the PDA chirp measurements due to the intense and short chirp pulse. Two examples of the line shape as a function of the timing relative to the UV pulse are shown in Fig. 13. Analysis of all measurements results in an XUV production timing of $+0.2(0.4)$ns relative to expectations based on the shape of the UV pulse and a $P_{\mathrm{XUV}} \sim P_{\mathrm{UV}}^{4.5}$ power dependence. The XUV pulse width is 3 ± 0.5ns. From this it can be concluded that the XUV is indeed produced in the most intense part of the UV pulse. Ionization in the nonlinear medium, which could limit XUV production to the leading edge of the UV pulse [54], is therefore not significant (see also Sec. III B 4).

B. Antichirp measurements

The effect of a counteracting phase modulation (antichirp) is shown in Fig. 14. Efforts to minimize the chirp concentrated on the central part of the UV pulse, where most of the signal is generated. The residual chirp has no strong influence on the resonance position due to its antisymmetric nature in the leading and trailing part of the pulse. Application of antichirp typically shifts the resonance between 65 and 90 MHz upward in frequency compared to the uncompensated situation, leaving a residual effect on the resonance position of 1–10 MHz. The difference between calculated and measured effect of antichirp on the resonance position is gener-

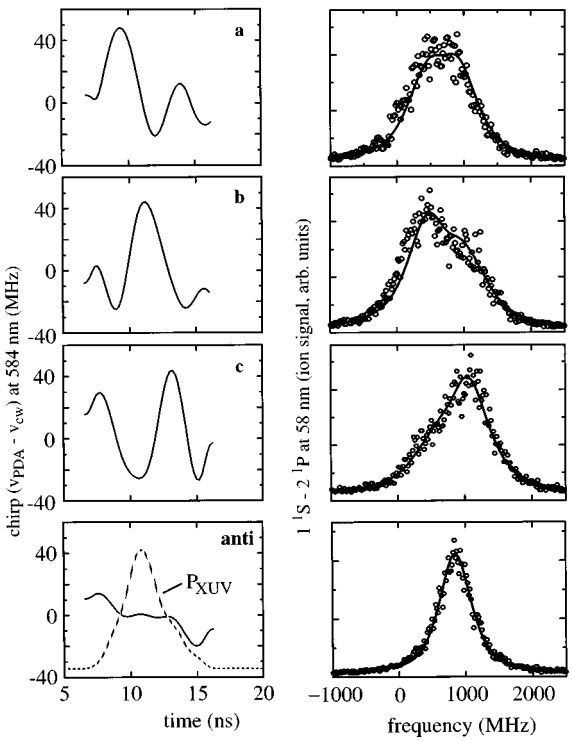

FIG. 12. Experimental and calculated $1\,^1S$-$2\,^1P$ transition line shape (right side, average over four scans) due to induced extra chirp (parts *a* to *c*) and antichirp (''anti'') (left side, average over 100 laser pulses). The frequency reference (''0'' MHz) is the position of the I_2 calibration and the dotted line in the lower trace is the estimated XUV power dependence on UV power.

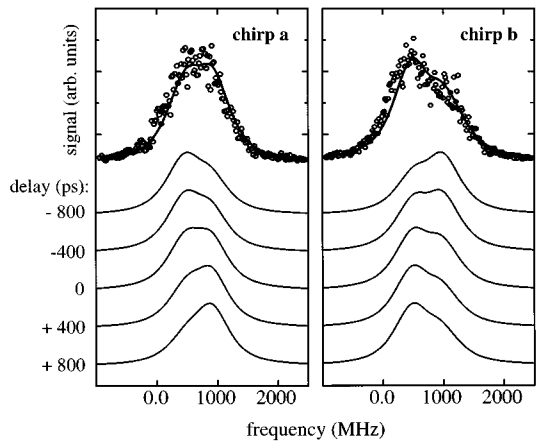

FIG. 13. Calculated line shape for chirp situations *a* and *b* of Fig. 12 for the $1\,^1S$-$2\,^1P$ transition as a function of the XUV production timing relative to what is expected based on the XUV-UV power dependence. From this analysis the temporal window of XUV production is derived (see text).

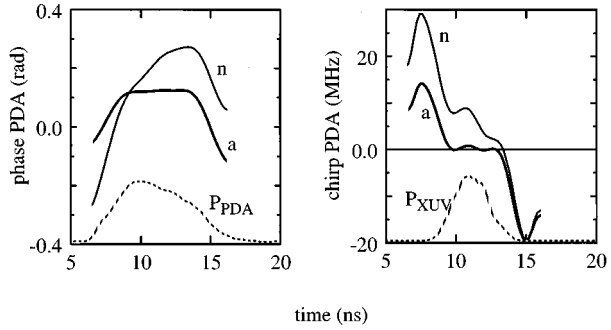

FIG. 14. Typical phase and chirp evolution for normal (n) and antichirped (a) PDA pulses (average over 10 pulses). The dotted lines represent the PDA pulse and estimated XUV pulse shape ($P_{XUV} \sim P_{UV}^{4.5}$). Note that under conditions of antichirp the reconstructed phase is constant and the frequency excursion close to zero during the time window of XUV generation.

ally within 10 MHz, confirming that the influence of chirp can be evaluated with good accuracy. Antichirp did not significantly reduce the transition linewidth due to the relatively small normal chirp. For the visible output of the PDA a bandwidth reduction could be achieved by applying antichirp over the total pulse. In this case the bandwidth reduced from $\sim$97 MHz to 92 MHz, still above the Fourier transform bandwidth of $\sim$78 MHz of those pulses due to pulse-to-pulse fluctuation in the chirp, which cannot be compensated.

Apart from uncertainties due to the chirp measurement procedure (10 MHz) and PDA beam inhomogeneities (20 MHz) a third error is introduced in calculating the effects of PDA chirp due to the uncertainty in XUV production timing (0.4 ns) and width (0.5 ns). The same parameters determine the effect of chirp in frequency doubling and harmonic generation. Therefore the combined uncertainty due to timing and width is calculated, resulting in an extra statistical error of 10 MHz of which 8 MHz is due to the PDA chirp. The calculated effect of the XUV width uncertainty is small ($\sim$1–2 MHz) because of the antisymmetric chirp in the measurements. In conclusion, an overall uncertainty of 14 MHz results from the chirp measurement procedure and calculations of its effect on the resonance position (see Table I).

C. The $1\,^1S$-$2\,^1P$ transition frequency

The measurement procedure started with seven recordings using the He/Kr mixture in the interaction zone, followed by seven with pure helium, all under normal chirp conditions. From these measurements a Doppler shift of $-7(20)$ MHz was determined. Then 25 measurements with antichirp were performed and corrected for the residual chirp in the XUV of typically 1–10 MHz. In Fig. 15 a typical recording of the $1\,^1S$-$2\,^1P$ transition under antichirp conditions is shown, together with etalon and I_2 calibration spectra. In Fig. 16 the measured resonance frequency is shown as a function of the measurement time, including all measurements except those with pure helium. After several hours of measurements a drift became apparent, which could be reproduced in a second series of measurements at a later time of which only the accurate normal and antichirped values are shown in the right part of Fig. 16 (in between ''extra-chirp'' measurements were performed). Nothing was changed between these

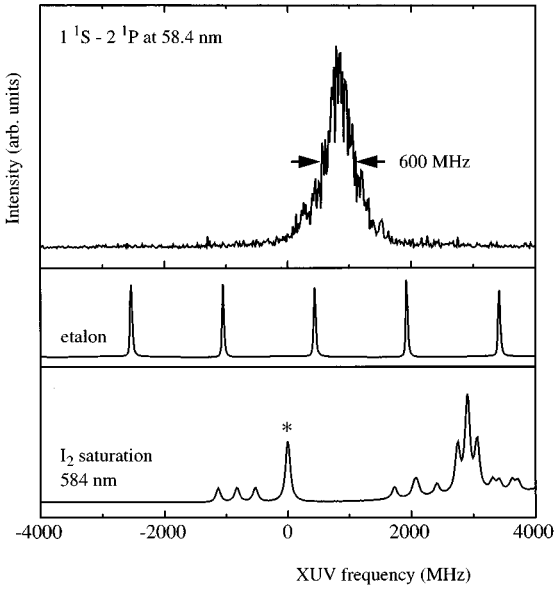

FIG. 15. The $1\,^1S$-$2\,^1P$ resonance transition for antichirped PDA pulses with etalon and I_2 saturated absorption spectrum. The asterisk indicates the ''o'' component of the P88(15-1) transition which was used for absolute calibration.

two measurement series, except that the pump laser was switched off for several hours. Because chirp and UV intensity were monitored regularly this drift is ascribed to Doppler effects, probably due to thermal drift in the Nd:YAG laser intensity profile that influences the UV beam. Therefore, the $1\,^1S$-$2\,^1P$ average transition frequency of 5 130 495 110(5) MHz was determined from a weighted average over the first 18 measurements (including 7 with normal chirp, but chirp corrected) for which the drift had an influence of less than 3 MHz. Inclusion of all measurements would result in a 10 MHz lower resonance frequency. To account for possible residual drifts we included a systematic error of 3 MHz in the error budget (Table I).

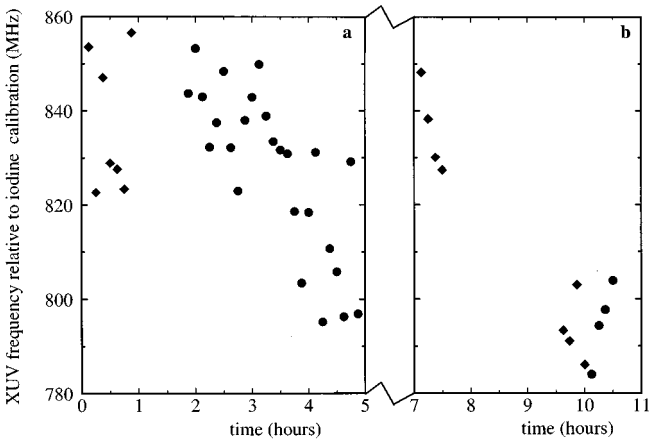

FIG. 16. Drift of the resonance position in time due to indirect Doppler effects. Only the accurate chirp-corrected normal and antichirped measurements are shown using the He/Kr mixture. In between the measurement of both series the Nd:YAG laser was switched off.

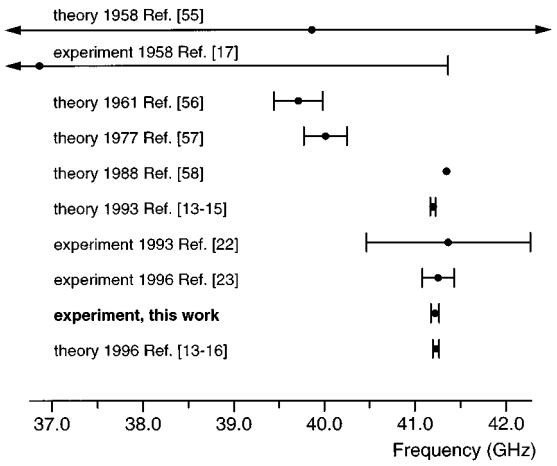

FIG. 17. Measurements of the $1\,^1S$ Lamb shift and developments in theory. The experimental value of Ref. [17] has been deduced using the measured wavelength of the $1\,^1S$-$2\,^1P$ transition and the most recent evaluation of the non-QED terms. The uncertainty in the theoretical value in Ref. [55] is 6 GHz. Reference [58] does not contain an estimate of the error.

The last correction of $-44(15)$ MHz for the dynamic Stark shift in the resonance transition of ^{4}He was determined from a separate run as described in Sec. III C 1. In Table I the results are summarized, together with the corrections and uncertainties. For completeness the previously determined isotope shift of 263 410(7) MHz [23] is included in Table I as well (see Sec. III C 2 and Appendix for the Stark shift difference correction). The final value for the $1\,^1S$-$2\,^1P$ transition frequency for ^{4}He is 5 130 495 083(45) MHz.

V. DISCUSSION

The present investigation with a tunable XUV laser system resulted in a determination of the absolute frequency of the $1\,^1S$-$2\,^1P$ transition in helium, with a precision better than 1 part in 10^8. From the measured frequency of 5 130 495 083(45) MHz and the calculations for the non-QED level energies [13–16] a value of 41 224(45) MHz for the Lamb shift in the ground state is deduced. In Fig. 17 existing experimental and calculated data on the $1\,^1S$ Lamb shift are collected. This plot reflects not only the recent progress in experimental accuracy but also the time evolution in the theoretical value. The transition isotope shift ^{4}He-^{3}He was determined to be 263 410(7) MHz. From these measurements more accurate values for the ionization energies of the helium atom can be deduced: 198 310.6672(15) cm^{-1} for ^{4}He and 198 301.8808(15) cm^{-1} for ^{3}He.

As can be seen in Table I and Fig. 17 both isotope shift and absolute frequency of the $1\,^1S$-$2\,^1P$ transition are in excellent agreement with the latest theoretical predictions. The accuracy in the theoretical isotope shift is significantly higher than that for the absolute transition frequencies. This is due to the cancellation of nearly equal QED contributions in both isotopes. In principle from an isotope shift measurement the nuclear charge radius of ^{3}He with respect to the more accurately known charge radius of ^{4}He may be deduced. This was recently shown by Shiner *et al.* [59] using highly accurate measurements in the $2\,^3S$-$2\,^3P$ transition. Our $1\,^1S$-$2\,^1P$ isotope shift measurement, although it constitutes the most precise experiment in the XUV spectral region, is not yet sufficiently accurate for this purpose.

TABLE II. Contributions to the negative ionization energies of ^{4}He (in MHz).

Term	$1\,^1S_0$	$2\,^1P_1$
$E_{\text{non-QED}}$	−5 945 162 994	−814 709 115.82
$E_{L(1)}$	45 441 (35)	100.3 (1.8)
$E_{L(2)}$	−4208	−62.82
$(E_{L(1)}+E_{L(2)})$	(41 233)	(37.5)
total	−5 945 204 227 (35)	−814 709 153.3 (1.8)
	$E_{L(1)}$ composition	
Term	$1\,^1S_0$	$2\,^1P_1$
α^3Z^4	44 702.27	100.50
Bethe log. corr.	6.73 (4)	−1.8(1.8)
α^4Z^5	771.11	1.66
$\alpha^4Z^3\ln(\alpha)$	30.67	0.21
α^5Z^6	−68.8 (35.)	−0.09
two-loop	6.88	0.02
two-loop binding	−3.95	−0.01
finite mass	−4.05	−0.18
total	45 440.9 (35.)	100.3(1.8)

The absolute frequency measurement given in Table I allows for an interesting comparison with theory. Experiment and theoretical calculations now show the same level of accuracy for the Lamb shift of the $1\,^1S$ ground state. The theoretical Lamb shift has a value of 41 233(35) MHz which follows from the accurately known theoretical energy position of $2\,^1P_1$ and the non-QED energies in the ground state [13–16], shown in Table II. Theoretically the Lamb shift contains two-electron generalizations of the well known one-electron effects in hydrogen, and electron-electron contributions (not present in hydrogen), that explicitly depend on the inter-electronic distance. Calculations of the one-electron part $E_{L(1)}$ are similar to that in hydrogen, but a correction is applied to account for the influence of the second electron on the electron density at the nucleus [13,15]. Because the operators describing the two-electron Lamb shift $E_{L(2)}$ are known explicitly this term can in principle be calculated with high precision. Higher-order corrections of order α^4Z^4 to $E_{L(2)}$ have not been evaluated yet; however, a great deal of cancellation is suspected in these terms for helium [16]. As a result the uncertainty in the theoretical $1\,^1S$ Lamb shift is completely determined by $E_{L(1)}$ in the ground state as the 1.8 MHz theoretical uncertainty in the $2\,^1P$ level (due to the two-electron contribution to the Bethe logarithm [15,16]) is negligible in this respect.

The terms of order α^4Z^5 and α^5Z^6 in $E_{L(1)}$ are of special interest. Both were calculated using unscreened hydrogenic values with a correction for the electron density at the nucleus [15,16]. Given the size of these contributions [771.11 MHz from $O(\alpha^4Z^5)$ and −68.8 MHz from $O(\alpha^5Z^6)$] this appears to be a very good approximation

given the excellent agreement between experiment and theory. A similar agreement was found for the $2\,^3S$ level in Li^+ [60], and for the $2\,^1S$ level in helium. Comparing the calculations for $2\,^1S$ shows that terms of order $O(\alpha^4 Z^5)$ contribute 51.99 MHz to the Lamb shift of the $2\,^1S$ state, whereas they shift the $1\,^1S$ state 771.11 MHz. The leading correction to these values was recently calculated by Drake *et al.* [15,16]. This term of $O(\alpha^4 Z^3 \ln\alpha)$, which is an order of magnitude smaller than the leading two-electron term, adds 2.49 MHz in the $2\,^1S$ case and 30.67 MHz in the $1\,^1S$. Residual two-electron corrections of $O(\alpha^4 Z^4)$ are expected to be smaller but still remain to be calculated. They may contribute at the 10 MHz level to the shift of the $1\,^1S$ state. For the present estimate of the theoretical accuracy these terms are neglected as uncalculated $O(\alpha^5 Z^6)$ corrections are expected to be larger [15,16]. Two-electron corrections to the $\alpha^5 Z^6$ term, which has a value of -68.8 MHz, are expected to be smaller in a $1/Z$ expansion by a factor of 2, resulting in a theoretical uncertainty of 35 MHz. The order of magnitude estimate of the error in the theoretical $1\,^1S$ Lamb shift thus is dominated by this 35 MHz [15,16].

VI. CONCLUSION AND OUTLOOK

In the present work it has been demonstrated that high-precision measurements are feasible at wavelengths in the XUV as short as 58 nm. The measurement of the $1\,^1S$-$2\,^1P$ transition in helium constitutes a test of QED effects in low-energy physics. It is a stringent test because the experimental accuracy of 45 MHz is comparable to the estimated uncertainty in the calculation of QED effects in the helium ground state. Excellent agreement is found between theory and experiment. Expected improvements in calculations of the ground state Lamb shift in the near future, by evaluation of higher order terms in the $Z\alpha$ expansion, raise the question whether the experimental accuracy may be improved as well.

For the $1\,^1S$-$2\,^1P$ transition no immediate improvements are foreseen. The uncertainties related to Doppler shift, Stark shift, and chirp are of the same order of magnitude, which implies that all three would have to be reduced to gain in precision. In view of the 286 MHz natural linewidth of $2\,^1P$ excited state further reduction of the bandwidth of the XUV source will have no beneficial effects on precision. Improvement may be expected from two-photon excitation of the $1\,^1S$-$2\,^1S$ transition at 120 nm (sixth harmonic of 720 nm), which has several advantages: possibility of Doppler-free excitation, a smaller dynamic Stark shift, and an upper state lifetime of 3 ms. Thus in a two-photon scheme several uncertainties, contributing to the error budget of the one-photon excitation, are significantly decreased. However, limitations imposed by the frequency bandwidth of the VUV pulses and by chirp phenomena are not avoided in such a scheme.

The precision in a $1\,^1S$-$2\,^1S$ two-photon transition may be further improved by applying sequential phase-locked coherent VUV pulses. This technique derives from Ramsey's experiment on the hydrogen maser [61], in which phase-locked oscillatory microwave fields drive a transition in spatially separated zones. Ramsey's interference technique was extended to a technique of time-separated phase-locked oscillatory fields by Salour and Cohen-Tannoudji [62] for Q-switched laser pulse. Along these lines we propose to implement two time-separated phase-locked VUV pulses to induce the $1\,^1S$-$2\,^1S$ transition in helium. A geometry of counterpropagating VUV beams ensures that dephasing of interference fringes due to Doppler effects is circumvented (see also the review of Salour [63]).

The elegance of this spectroscopic method is that only the narrow spacing $\Delta\omega$ between fringes depends on the time delay T via $\Delta\omega = \pi/T$. The spectroscopic resolution is dramatically enhanced when the central fringe is resolved. Moreover, disturbing phenomena, such as asymmetries in the frequency profile and frequency chirp effects, only cause perturbations in the envelope of the fringe pattern. They have hardly any or no effect on the frequency position of the central fringe, which only depends on the locking of the separated pulses to the clock frequency of the carrier wave. The resolution in the experiment is determined by the coherence properties of the narrow-band seed laser, while pulse amplification provides the required power to generate the VUV and induce the two-photon transition. Implementation of all procedures mentioned above should produce an absolute accuracy of 1 MHz for the Lamb shift of the He 1^1S state.

An experiment to demonstrate the Ramsey interference technique in the VUV/XUV domain is in preparation in our laboratory. A subsequent goal is then to demonstrate the feasibility of the above proposed scheme.

ACKNOWLEDGMENTS

We gratefully acknowledge G. W. F. Drake for helpful remarks and the results of theoretical calculations prior to publication, and J. Bouma for his valuable technical contributions to the experiments. We acknowledge financial support from The Netherlands Foundation for Fundamental Research on Matter (FOM).

APPENDIX: DYNAMIC STARK SHIFT AND HYPERFINE STRUCTURE

Because of its hyperfine structure the dynamic Stark shift in ^{3}He is slightly smaller than in ^{4}He. In the case of random polarized UV and XUV radiation no difference in Stark shift would be observed. However, due to the parallel and linear polarization of XUV and UV the tensor polarizability of the $2\,^1P$ transition introduces a Stark shift difference. The combined effect of hyperfine structure and Stark shift is calculated by diagonalizing the Stark, fine, and hyperfine interactions together in the $1s2p$ configuration in a $|LSJIFM_F\rangle$ basis. The transition frequency for ^{4}He can be calculated directly from the dynamic scalar and tensor polarizabilities; for ^{3}He, however, the center of gravity has to be determined by integrating the Schrödinger equation that describes the coherent excitation of the unresolved $2\,^1P$ $F=\frac{1}{2}$ and $F=\frac{3}{2}$ hyperfine components.

Analogous to the treatment of Hinds *et al.* [64], the hyperfine structure of $2\,^1P_1$ is calculated by diagonalizing a matrix containing the interacting $2\,^1P_1$ and $2\,^3P_J$ states to include singlet-triplet mixing. The magnetic dipole and electric quadrupole hyperfine-structure matrix elements were taken from Riis *et al.* [60], with the interaction parameters for the $1s2p$ configuration $C_{s,s}$ (Fermi contact term), D_s

(nuclear spin orbit), and $E_{s,s}$ (nuclear spin-spin) as given by Marin *et al.* [65]. The fine-structure elements reported by Hinds *et al.* [64] were used to account for singlet-triplet mixing. The energy reference (= theoretical energy in the absence of hyperfine structure) is first determined by diagonalizing the fine structure matrix. Then a rediagonalization is performed including the hyperfine interaction, resulting in a hyperfine splitting of 41.63 MHz ($F=\frac{1}{2}$: +28.63 MHz and $F=\frac{3}{2}$: −13.00 MHz).

To include the effect of a dynamic Stark shift, it is convenient to express it in terms of scalar ($\alpha_{\rm sc}$) and tensor polarizabilities ($\alpha_{\rm ten}$) as used for static fields [66]. The conversion from a static to a dynamic Stark shift is performed by replacing the static field by the time-averaged squared electric-field amplitude $\overline{E^2}=1/2E^2=I/\varepsilon_0 c$ as well as a change in the energy difference denominator to include the energy of the field at frequency ω [67]. Also it has to be taken into account that the polarizations of the UV and XUV are linear and parallel, defining a z axis in the system. Starting from the ground state with $S=0$ the selection rules are $\Delta L=\Delta J=\pm 1$; $\Delta F=0,\pm 1$, and $\Delta m=0$. The first-order dynamic Stark shift of a level with an unshifted energy E_n for linear polarized light can then be written as

$$\Delta E_n=-\tfrac{1}{2}\alpha_{\rm sc}(J)\overline{E^2}-\tfrac{1}{2}\alpha_{\rm ten}(J)\overline{E^2}(-1)^{F-M_F}\begin{pmatrix} F & 2 & F' \\ -M_F & 1 & M_F\end{pmatrix}$$
$$\times(-1)^{I+J+F}\left(\frac{(2F+1)(2F'+1)(2J+3)(2J+2)(2J+1)}{2J(2J-1)}\right)^{1/2}\begin{Bmatrix} J & F & I \\ F' & J & 2\end{Bmatrix} \tag{A1}$$

with the polarizabilities expressed in terms of reduced matrix elements:

$$\alpha_{\rm sc}(J)=\frac{-2}{3\hbar(2J+1)}\sum_{\gamma' J'}(-1)^{J'-J}\frac{|\langle \gamma J\|\mu\|\gamma J'\rangle|^2\Delta\omega_{\gamma J,\gamma' J'}}{\Delta\omega^2_{\gamma J,\gamma' J'}-\omega^2} \tag{A2}$$

and

$$\alpha_{\rm ten}(J)=\frac{2}{\hbar}(-1)^{2J+1}\left(\frac{10}{3}\right)^{1/2}\left(\frac{2J(2J-1)}{(2J+3)(2J+2)(2J+1)}\right)^{1/2}$$
$$\times\sum_{\gamma' J'}(-1)^{J-J'}\begin{Bmatrix} 1 & 1 & 2 \\ J & J & J'\end{Bmatrix}$$
$$\times\frac{|\langle \gamma J\|\mu\|\gamma' J'\rangle|^2\Delta\omega_{\gamma J,\gamma' J'}}{\Delta\omega^2_{\gamma J,\gamma' J'}-\omega^2}. \tag{A3}$$

Here $\Delta\omega_{\gamma J,\gamma' J'}=(E_{\gamma J}-E_{\gamma' J'})/\hbar$. The summation over $\gamma' J'$ includes an integration over the ^1P continuum connected to the ground state, and ^1S and ^1D continua for $2\,^1P$. The dipole moments up to $n=21$ were deduced from oscillator strength calculations by Theodosiou [38] with an extrapolation to higher n based on an array oscillator-strength approximation [68], including quantum defects. Theoretical work of Goldberg [69] and Jacobs [47] and experiments of Chan *et al.* [70] were combined to obtain the dipole-moment density of the continua up to an energy of 2.4 Ry. Using these values to evaluate Eqs. (A2) and (A3) at 292 nm (carefully integrated around the pole in the continuum) results in $\alpha_{\rm sc}=0.057\times10^{-6}$ Hz V^2/m^2 for the ground state ($\alpha_{\rm ten}=0$ because $J=0$), and $\alpha_{\rm sc}=-1.446\times10^{-6}$ Hz V^2/m^2 and $\alpha_{\rm ten}=1.176\times10^{-7}$ Hz V^2/m^2 for $2\,^1P$ with an estimated accuracy of $\sim$10%.

The combined effect of dynamic Stark shift (at a specific UV power) and hyperfine structure is obtained by diagonalizing the total matrix in the F,M_F basis with $F=\frac{1}{2}$ and $F=\frac{3}{2}$. The diagonal elements contain the hyperfine level energies together with the Stark shift energy corresponding to the scalar polarizabilities. The only off-diagonal elements belong to the tensor polarizability which couples $F=\frac{1}{2}$ and $F=\frac{3}{2}$ with the same M_F. At a peak UV power of 25 MW/cm^2, used for the isotope shift measurements, the resulting eigenstates have mixed amplitudes of 0.981 (leading term) and 0.194 (admixture of other F state). The sign of the leading term is always chosen positive, to comply with sign conventions. The dipole moments for excitation can be obtained with the Wigner-Eckart theorem (see, e.g., Sobelman [71]), which are proportional to the reduced matrix element $\langle nL\|P\|n'L'\rangle$ since $S=0$ and $L=J$. This matrix element is the same for all intermediate states and therefore not important in this discussion. However, for the ionization step to the orthogonal ^1S and ^1D continua the difference in photoionization probability due to $|\langle nL\|\mu\|n'L'\rangle|^2$ [relative values 1 (for ^1S) and 12 (for ^1D) [47]] has to be included.

Although several theoretical papers have been published on the subject of interference in $1+1$ photon ionization (see, e.g., [72]) based on Bloch equations extended with a Raman type coupling to the continuum, here the simplified and more direct approach of Luk *et al.* [73], directly integrating the Schrödinger equation, is used. However, in our case the excitation and ionization steps overlap and therefore the integration has to be performed partially by numerical methods. The amplitudes of the ground state is denoted C_g, of the intermediate hyperfine levels C_n and of the final ion state C_f. In addition, $\Delta_{ng}=\omega_{ng}-\omega_x$ and $\Delta_{fn}=\omega_{fn}-\omega_u$ are defined with ω_{ng} and ω_{fn} being the transition frequencies and ω_x and $\omega_u(\omega_x=5\omega_u)$ the XUV and UV frequencies, respectively. The excitation process to the intermediate $2\,^1P$ levels can then be described by [74]

$$\frac{\mu_{ng}E_x}{\hbar}\cos(\omega_x t)e^{i\omega_{ng}t}C_g-i\Gamma C_n=i\frac{dC_n}{dt}. \tag{A4}$$

Γ is the fluorescence rate, equal for both F components. In the RWA approximation Eq. (A4) can be written as

$$\frac{\mu_{ng}E_x}{2\hbar}e^{i\Delta_{ng}t}C_g - i\Gamma C_n = i\frac{dC_n}{dt}. \tag{A5}$$

In the following its assumed that $C_g \sim 1$, a reasonable assumption because the estimated XUV power density of $\sim 25\ \mathrm{mW/cm^2}$ is much lower than the saturation power of the transition ($190\ \mathrm{W/cm^2}$). Also it is assumed that the ionization process can be taken as a perturbation, based on the estimated XUV and UV power levels (only a few percent ionization). To simplify the integration square laser pulses of duration $t = 3$ ns are used. This approximation only changes the transition linewidth but is not expected to influence the center of gravity significantly. The amplitude of the intermediate states is

$$C_n(\omega_x, t) \approx \beta_n \frac{(\mu_{ng}E_x/2\hbar)(1 - e^{i\Delta_{ng}t})}{\Delta_{ng} - i\Gamma}, \tag{A6}$$

where β_n has been included to account for the relative signs of the intermediate hyperfine level wave functions (mixture of $F = \frac{1}{2}$ and $F = \frac{3}{2}$ due to Stark effect). Phase evolution differences of the intermediate states wave functions can be ignored because of the short interaction time compared to the level splittings. When ionization again is assumed to be a small perturbation, the procedure for Eqs. (A4)–(A6) can be repeated resulting in a total ionization signal proportional to

$$|C_f(\omega_x, t)|^2 \propto E_x^2 E_u^2 \sum_{M_F} \sum_{\text{continua}} \int_{\omega_{fn}} \left| \sum_n \mu_{fn}\beta_n\mu_{ng}\,\eta(\Delta_{ng}, \Delta_{fn}, t) \right|^2 \tag{A7}$$

with

$$\eta(\Delta_{ng}, \Delta_{fn}, t) = \frac{1 - e^{i\Delta_{fn}t}}{(\Delta_{ng} - i\Gamma)\Delta_{fn}} - \frac{1 - e^{i(\Delta_{fn} + \Delta_{ng})t}}{(\Delta_{ng} - i\Gamma)(\Delta_{ng} - \Delta_{fn})}, \tag{A8}$$

where μ_{fn} denotes the dipole moment density, connecting intermediate and final state. The integration over the continuum states [with ω_{fn} as variable; integration over a limited range symmetrically around the poles in Eq. (A8) because only the relative transition amplitudes due to the intermediate levels are of interest] and the summation over the ^1S and ^1D continua, intermediate states n, and equally populated $M_F = \pm\frac{1}{2}$ states was performed numerically. The different continua (and different electron energies) do not interfere because they represent orthogonal final states when all electrons are detected over 4π [72,73]. This condition is automatically fulfilled when detecting the resulting ions.

The result for $25\ \mathrm{MW/cm^2}$ is a transition frequency for ^{3}He that is 6 MHz lower than that for ^{4}He (see Sec. III C 2).

[1] W. E. Lamb and R. C. Retherford, Phys. Rev. **72**, 241 (1947).

[2] W. E. Lamb and R. C. Retherford, Phys. Rev. **79**, 549 (1950); **81**, 222 (1951).

[3] G. W. F. Drake, Adv. At. Mol. Phys. **18**, 399 (1982).

[4] K. Pachucki, Phys. Rev. Lett. **72**, 3154 (1994).

[5] M. Weitz, A. Huber, F. Schmidt-Kaler, D. Leibfried, W. Vassen, C. Zimmermann, K. Pachucki, T. W. Hänsch, L. Julien, and F. Biraben, Phys. Rev. A **52**, 2664 (1995).

[6] S. Bourzeix, B. de Beauvoir, F. Nez, M. D. Plimmer, F. de Tomasi, L. Julien, F. Biraben, and D. N. Stacey, Phys. Rev. Lett. **76**, 384 (1996).

[7] G. W. F. Drake, *Advances in Atomic Molecular Physics*, edited by D. Bates and B. Benderson (Academic, New York, 1993), Vol. 31, p. 1.

[8] M. I. Haftel and V. B. Mandelzweig, Phys. Rev. A **49**, 3338 (1994); **49**, 3350 (1994).

[9] F. S. Pavone, F. Marin, P. De Natale, M. Inguscio, and F. Biraben, Phys. Rev. Lett. **73**, 42 (1994).

[10] D. Shiner, R. Dixon, and P. Zhao, Phys. Rev. Lett. **72**, 1802 (1994).

[11] C. J. Sansonetti and J. D. Gillaspy, Phys. Rev. A **45**, R1 (1992).

[12] W. Lichten, D. Shiner, and Z. X. Zhou, Phys. Rev. A **43**, 1663 (1991).

[13] G. W. F. Drake, I. B. Khirplovich, A. I. Milstein, and A. S. Yelkhovsky, Phys. Rev. A **45**, R15 (1993).

[14] J. D. Baker, R. C. Forrey, J. D. Morgan III, and R. N. Hill, Bull. Am. Phys. Soc. **38**, 1127 (1993).

[15] G. W. F. Drake, in *Long-Range Casimir Forces: Theory and Recent Experiments on Atomic Systems*, edited by F. S. Levin and D. A. Micha (Plenum, New York, 1993).

[16] G. W. F. Drake (private communication).

[17] G. Herzberg, Proc. R. Soc. London, Ser. A **248**, 309 (1958).

[18] W. Jamroz and B. P. Stoicheff, in *Progress in Optics*, edited by E. Wolf (North-Holland, Amsterdam, 1983), Vol. XX, p. 327.

[19] G. Hilber, A. Lago, and R. Wallenstein, J. Opt. Soc. Am. B **4**, 1753 (1987).

[20] E. Cromwell, T. Trickl, Y. T. Lee, and A. H. Kung, Rev. Sci. Instrum. **60**, 2888 (1989).

[21] J. J. Macklin, J. D. Kmetec, and C. L. Gordon III, Phys. Rev. Lett. **70**, 766 (1993).

[22] K. S. E. Eikema, W. Ubachs, W. Vassen, and W. Hogervorst, Phys. Rev. Lett. **71**, 1690 (1993).

[23] K. S. E. Eikema, W. Ubachs, W. Vassen, and W. Hogervorst, Phys. Rev. Lett. **76**, 1216 (1996).

[24] M. S. Fee, K. Danzmann, and S. Chu, Phys. Rev. A **45**, 4911 (1992).

[25] N. Melikechi, S. Gangopadyay, and E. E. Eyler, J. Opt. Soc. Am. B **11**, 2402 (1994).

[26] C. Wieman and T. W. Hänsch, Phys. Rev. A **22**, 192 (1980).

[27] K. Danzmann, M. S. Fee, and S. Chu, Phys. Rev. A **39**, 6072 (1989).

[28] R. G. Beausoleil, D. H. McIntyre, C. J. Foot, E. A. Hildum, B.

Couillaud, and T. W. Hänsch, Phys. Rev. A **35**, 4878 (1987).
[29] M. S. Fee, S. Chu, A. P. Mills, Jr., R. J. Chichester, D. M. Zuckerman, E. D. Shaw, and K. Danzmann, Phys. Rev. A **48**, 192 (1993).
[30] R. Grieser, G. Bönsch, S. Dickopf, G. Huber, R. Klein, P. Merz, A. Nicolaus, and H. Schnatz, Z. Phys. A **348**, 147 (1994).
[31] L. Hlousek and W. M. Fairbank, Jr., Opt. Lett. **8**, 322 (1983).
[32] J. Reintjes, *Nonlinear Optical Parametric Processes in Liquids and Gases* (Academic, New York, 1984).
[33] J. Reintjes, C.-Y She, and R. C. Eckardt, IEEE J. Quantum Electron. **14**, 581 (1978).
[34] A. Lago, G. Hilber, and R. Wallenstein, Phys. Rev. A **36**, 3827 (1987).
[35] D. S. Bethune and C. T. Rettner, IEEE J. Quantum Electron. **23**, 1348 (1987).
[36] M. Lewenstein, Ph. Balcou, M. Yu. Ivanov, A. L'Huillier, and P. B. Corkum, Phys. Rev. A **49**, 2117 (1994).
[37] D. Proch and T. Trickl, Rev. Sci. Instrum. **60**, 715 (1989).
[38] C. E. Theodosiou, Atom. Data Nucl. Data Tables **36**, 98 (1987).
[39] J. Larsson, E. Mevel, R. Zerne, A. L'Huillier, C.-G. Wahlström, and S. Svanberg, J. Phys. B **28**, L3 (1995).
[40] G. Scoles, *Atomic and Molecular Beam Methods* (Oxford University Press, New York, 1988).
[41] S. C. Rae, K. Burnett, and J. Cooper, Phys. Rev. A **50**, 3438 (1994).
[42] S. Gangopadhyay, N. Melikechi, and E. E. Eyler, J. Opt. Soc. Am. B **11**, 231 (1994).
[43] P. N. Butcher and D. Cotter, *The Elements of Nonlinear Optics* (Cambridge University Press, Cambridge, 1990).
[44] R. A. Haas and M. D. Rotter, Phys. Rev. A **43**, 1573 (1991).
[45] I. Reinhard, M. Gabrysch, B. Fischer van Weikersthal, K. Jungmann, and G. zu Putlitz, Appl. Phys. B **63**, 467 (1996).
[46] R. W. Boyd, *Nonlinear Optics* (Academic, London, 1992).
[47] V. L. Jacobs, Phys. Rev. A **9**, 1938 (1974).
[48] W. H. Press, A. S. Teukolsky, W. T. Vetterling, and B. P. Flannery, *Numerical Recipes*, 2nd ed. (Cambridge University Press, Cambridge, 1992).
[49] A. V. Smith and M. S. Bowers, J. Opt. Soc. Am. B **12**, 49 (1995).
[50] R. A. Adair, L. L. Chase, and S. A. Payne, Phys. Rev. B **39**, 3337 (1989).
[51] M. Sheik-Bahae, D. Crichton Hutchings, D. J. Hagan, and E. W. Van Stryland, IEEE J. Quantum Electron. **27**, 1296 (1991).
[52] M. Lewenstein, P. Salières, and A. L'Huillier, Phys. Rev. A **52**, 4747 (1995).
[53] D. M. Mittleman, D. C. Douglass, Z. Henis, O. R. Wood II, R. R. Freeman, and T. J. McIlrath, J. Opt. Soc. Am. B **13**, 170 (1996).
[54] J. E. Muffett, C-G Wahlström, and M. H. R. Hutchinson, J. Phys. B **27**, 5693 (1994).
[55] P. K. Kabir and E. E. Salpeter, Phys. Rev. **108**, 1256 (1957); J. Sucher, *ibid.* **109**, 1010 (1958).
[56] C. Schwartz, Phys. Rev. **123**, 1700 (1961).
[57] K. Aashamar and A. Austvik, Phys. Norv. **8**, 229 (1977).
[58] G. W. F. Drake, Nucl. Instrum. Methods B **31**, 7 (1988).
[59] D. Shiner, R. Dixon, and V. Vedantham, Phys. Rev. Lett. **74**, 3553 (1995).
[60] E. Riis, A. G. Sinclair, O. Poulsen, G. W. F. Drake, W. R. C. Rowley, and A. P. Levick, Phys. Rev. A **49**, 207 (1994).
[61] N. F. Ramsey, Phys. Rev. **76**, 996 (1949).
[62] M. M. Salour and C. Cohen-Tannoudji, Phys. Rev. Lett. **38**, 757 (1977).
[63] M. M. Salour, Rev. Mod. Phys. **50**, 667 (1978).
[64] E. A. Hinds, J. D. Prestage, and F. M. J. Pichanick, Phys. Rev. A **32**, 2615 (1985).
[65] F. Marin, F. Minardi, F. S. Pavone, M. Inguscio, and G. W. F. Drake, Z. Phys. D **32**, 285 (1995).
[66] J. R. P. Angel and P. G. H. Sandars, Proc. R. Soc. A **305**, 125 (1968).
[67] H. Friedrich, *Theoretical Atomic Physics* (Springer-Verlag, Berlin, 1990).
[68] R. D. Cowan, *The Theory of Atomic Structure and Spectra* (University of California Press, Berkeley, 1981).
[69] L. Goldberg, Astrophys. J. **90**, 414 (1939).
[70] W. F. Chan, G. Cooper, and C. E. Brion, Phys. Rev. A **44**, 186 (1991).
[71] I. I. Sobelman, *Atomic Spectra and Radiative Transitions* (Springer-Verlag, Berlin, 1979).
[72] A. T. Georges and P. Lambropoulos, Phys. Rev. A **18**, 1072 (1978).
[73] T. S. Luk, L. Dimauro, M. Feldman, and H. Metcalf, Phys. Rev. A **24**, 864 (1981).
[74] R. Loudon, *The Quantum Theory of Light*, 2nd ed. (Clarendon, Oxford, 1983).